



Smart4RES

Methodologies for short-term solar resource forecasting by merging various inputs

D2.3. Methodologies for short-term solar resource forecasting by merging various inputs

WP2, T2.3

Version V2.0

Authors: Jorge Lezaca (DLR VE), Niklas Blum (DLR SF), Bijan Nouri (DLR SF), Annette Hammer (DLR VE), Ontje Lündsdorf (DLR VE)



Disclaimer

The present document reflects only the author's view. The European Climate, Infrastructure and Environment Executive Agency (CINEA) is not responsible for any use that may be made of the information it contains.

Technical references

Project Acronym	Smart4RES
Project Title	Next Generation Modelling and Forecasting of Variable Renewable Generation for Large-scale Integration in Energy Systems and Markets
Project Coordinator	ARMINES – MINES ParisTech
Project Duration	November 2019 – April 2023

Deliverable	D2.3. Methodologies for short-term solar resource forecasting by merging various inputs
Dissemination level ¹	PU
Nature ²	R
Work Package	WP2 – Next Generation of Weather Forecasting Models for RES Purpose
Task	T 2.3 – Short-term solar resource forecasting by merging various inputs
Lead beneficiary	DLR
Contributing beneficiary(ies)	DLR
Reviewers	Heidrun Misfeld (EMSYS) Tuhfe Göçmen (DTU)
Due date of deliverable	01 10 2021 (delayed of 6 months)

- ¹ PU = Public
PP = Restricted to other program participants (including the Commission Services)
RE = Restricted to a group specified by the consortium (including the Commission Services)
CO = Confidential, only for members of the consortium (including the Commission Services)
- ² R = Report, P = Prototype, D = Demonstrator, O = Other

Document history		
V	Date	Description
0.1	13/04/2022	First draft submitted by Jorge Lezaca
0.2	28/04/2022	Reviews by Heidrun Misfeld (EMSYS) and Tuhfe Göçmen (DTU)
1.0	28/04/2022	Revised Version
2.0	29/04/2022	Final version submitted to the European Commission

1 Executive summary

Nowcasts from all sky imagers (ASIs) can reach a spatial resolution of down to $5\text{ m} \times 5\text{ m}$ and can provide nowcasts for lead times of 0 to 15 min (Nouri et al., 2020b). Nowcasts of solar irradiance based on up to four ASIs located in proximity have been demonstrated experimentally (Nouri et al., 2018; Peng et al., 2015). So far, such nowcasts have been applied mainly to predict the production of the solar power plants in which they were located. Compared to ASI nowcasts, satellite based forecasts present a much higher spatial and temporal coverage in detriment of a lower resolution. Today, these forecasts can be processed for any region included in the satellite view with a $1\text{ km} \times 1\text{ km}$ resolution at the equator and with a temporal resolution of 5 to 15 min.

An urban distribution grid can cover an area of e.g. $13\text{ km} \times 12\text{ km}$. Typically, it features numerous photovoltaic installations with a name plate capacity of 10 to 30 kW. Conventional ASI-based nowcasting systems are often used to nowcast the production of a single PV plant located close to the ASIs. Compared to this case, a conventional ASI-based nowcasting system with 2 to 4 ASIs is expected to be less accurate if the production of these distributed installations needs to be nowcasted. This motivates the use of an enhanced evaluation which combines individual ASIs and ASI pairs into an ASI network. The Eye2Sky ASI network provides the experimental infrastructure for these combination tasks. At the time of the experiment, Eye2Sky incorporated 12 ASIs in the urban area of Oldenburg and a sparser setup of 11 ASIs in its rural environment of $110\text{ km} \times 100\text{ km}$. This spatial extent turns out to be a very well suited test case to assess the advantages that a combination between the highly resolved ASI network nowcast and the high coverage satellite forecast brings to the overall forecasting performance.

An enhanced method is developed which allows to evaluate Eye2Sky's distributed ASIs in combination in the sense of an ASI network. For this, the workflow of a state-of-the-art ASI-based nowcast (e.g. Nouri et al., 2020b) is followed. The various intermediate products of an ASI-based nowcast (cloud height, cloud segmentation, cloud velocity and diffuse irradiance) are merged between all available data sources by dedicated statistical procedures. This way, we aim to mitigate errors and to extend the spatial and temporal coverage of the nowcast. The results of the ASI network are validated in comparison to a state-of-the-art ASI pair and a persistence nowcast. Depending on the evaluated station, the ASI network reduces Root Mean Square Deviation (RMSD) by 23-30% ($35 - 50\text{ W/m}^2$), 15-21% ($25 - 37\text{ W/m}^2$), 12-16% ($20-27\text{ W/m}^2$), 8-12% ($14 - 21\text{ W/m}^2$) over persistence at evaluated lead times of 5, 10, 15, 20 min. The ASI network's advantage over the ASI pair and persistence increases in particular if more peripheral locations are evaluated. As to be expected, the ASI-based approaches bring a larger improvement over persistence in more variable atmospheric conditions. In these more variable conditions, the ASI network reduces RMSD by up to 36% and up to 75 W/m^2 over persistence. The ASI network's nowcast is also evaluated for higher lead times. Up to a lead time of 95 min, the ASI network has a lower RMSD than persistence.

A second method to combine the highly resolved ASI network nowcast with the satellite-based forecast was developed. The method uses a linear regression to find optimal weights to combine the forecast inputs in such a way that the average error metrics are minimized with respect to ground measurements. Using historical forecasts, the linear regression of the combination indirectly characterizes the mean local weather conditions that influence the forecast accuracy. We found that this newly developed hybrid forecast outperforms the RMSD of persistence and the individual input forecasts for all lead times calculated. It shows an improvement on RMSD of 5.07% to 13.97% with respect to satellite forecasts and 7.55% to 15.09% with respect to the ASI network forecast on lead times going from 5 to 30 min. It also shows a better RMSE on highly variable conditions.

Key messages:

- An all-sky imager (ASI) network is developed to nowcast solar irradiance for lead times of up to two hours
- The ASI network's RMSD is frequently 25% lower than the one of the state-of-the-art ASI-based reference nowcast, depending on location, lead time and atmospheric conditions.
- The hybrid forecast obtained with the combination of an ASI network nowcast with a satellite forecast outperforms the RMSD of persistence and the individual input forecasts for all lead times calculated.

The outcomes of this work package have been published partly in journal articles (Blum et al. 2021, Nouri et al. 2021, Blum et al. 2022, Fabel et al. 2022) and further publications are under preparation.

2 Table of contents

1	Executive summary	4
2	Table of contents	6
3	LIST OF TABLES	8
4	LIST OF FIGURES	9
1	Introduction	11
1.1	Context.....	11
1.2	Objectives.....	11
1.3	Contributions	12
2	Overview of the methodology.....	13
3	Advanced analysis of camera images for cloud characterization.....	14
3.1	Introduction	14
3.2	Case studies.....	14
3.3	Methodology	16
3.3.1	Estimating cloud height	16
3.3.2	Identifying the spatial distribution of cloud attenuation.....	16
3.3.3	Spatial variability of diffuse irradiance	18
3.3.4	Estimating cloud velocity and tracking clouds	19
3.4	Results and Discussion	19
3.4.1	Benchmarking the overall performance.....	19
3.4.2	Investigating the influence of DNI variability on nowcasting performance.....	22
3.4.3	Nowcasting errors at increased lead times	24
4	Highly resolved combined ASI network, satellite forecast and NWP forecast.....	26
4.1	Motivation	26
4.2	Case studies.....	26
4.3	Methodology	29
4.3.1	Description	29
4.3.2	Forecast homogenization	30
4.3.3	Regression and prediction	30
4.4	Evaluation	31
4.5	Results and Discussion	32
4.5.1	Benchmarking of the input forecasts on the Eye2sky region	32
4.5.2	Benchmarking of the combined Satellite + ASI network forecast on the Eye2sky region	35
4.5.3	Benchmarking of the performance of the forecasts with respect to the variability condition	38

4.5.4	Correlation of increments as a qualitative variability measurement	42
5	Conclusion	44
6	Key messages and recommendations	46
7	Bibliography	47
8	Appendix A: Summary of Smart4RES KPIs	49
8.1	Project KPIs.....	49
8.1.1	Forecasting KPIs.....	49
8.1.2	KPIs on grid management applications.....	50
8.1.3	KPIs on market applications.....	51

3 LIST OF TABLES

Table 1. Dataset used for the development and validation of the ASI network.....	14
Table 2. Datasets used for the development and for the validation of the nowcast.	15
Table 3. Five cloud classes received from cloud segmentation are mapped to values of the attenuation index AI.....	17
Table 4. This table summarizes the sky conditions indicated by each of the eight DNI variability classes according to Nouri et. al. 2021.	22
Table 5. Available forecasts.....	27
Table 6. Validation ground dataset.....	28
Table 7. Characteristics of the obtained Satellite + ASI network forecast.	32
Table 8. RMSE per forecast for selected lead times + relative improvement of nMAE of Satellite + ASInet over only SAT and only ASInet. The underlined values represent the minimum RMSE improvement per lead time taking both forecast inputs into account (worst case improvement)	36
Table 9. MAE per forecast for selected lead times + relative improvement of nMAE of Satellite + ASInet over only SAT and only ASInet. The underlined values represent the minimum MAE improvement per lead time taking both forecast inputs into account (worst case improvement)	37
Table 10: Smart4RES Forecasting KPIs	49
Table 11: Smart4RES Grid management KPIs	50
Table 12: Smart4RES Market applications KPIs	51

4 LIST OF FIGURES

Figure 1. Overview of the data flow between the different parts of this deliverable..... 13

Figure 2. Eye2sky Network overview. **Camera** stations (blue circles) are camera only stations, **Meteo** stations (brown circles) are camera + meteorological stations equipped with an RSI and **Reference** (green circles) are only meteorological stations equipped with thermal radiometers + solar tracker..... 15

Figure 3. The accuracy-weighted merging procedure is shown exemplarily with only two ASIs for 05 June 2020, 10:22:00. Each ASI delivers a georeferenced map of attenuation index AI_i (left column); the map of AI from each ASI is weighted by $ui - 1$ (center column), the inverse of the expected local uncertainty of AI_i ; the weighted average based on $AI_i ui - 1$ from all included ASIs yields the merged map of AI. 17

Figure 4. An exemplary map of DHI in the urban area of Oldenburg on 10 July 2020 13:00:00 (UTC) is shown. RSI station DON (x) and all ASIs in the urban area (o) provide a measurement of DHI to the nowcast. The RSIs at UOL and CLO (o) are used as references for the validation. .. 18

Figure 5. Deviations of the ASI-network-, ASI-pair- and persistence-based nowcasts of GHI for the locations DON (top), UOL (middle) and CLO (bottom) are evaluated over the 92-days validation dataset and are characterized by the metrics RMSD, MAD and bias..... 21

Figure 6. The RMSD of the ASI-pair- and ASI-network-based GHI nowcast for DON is plotted over the lead time for each of the eight DNI variability classes. The present DNI variability class is determined from the DNI measured by RSI DON in the 15 min preceding the respective forecast instance time. 23

Figure 7. This map shows the transformer district (orange solid shape) for which average GHI is nowcasted in Section 3.4.3. RSI DON (x) provides the reference measurements. The modeled transformer district is imaginary but has the same shape as a real transformer district in the center of Oldenburg (blue dashed shape). (background © OpenStreetMap contributors 2022. Distributed under a Creative Commons BY-SA License.) 24

Figure 8. Deviation metrics RMSD (o), MAD (o) and bias (+) are plotted for the persistence nowcast (blue) and for the ASI network nowcast (red). Unlike Figure 5, this evaluation is restricted to 25 days but covers lead times of up to 130 min. The deviation metrics evaluate 5-min average GHI from RSI DON and 5-min average GHI aggregated over the area of the transformer district shown in Figure 7..... 25

Figure 9. Combination model 29

Figure 10. Forecast step and forecast instance interpolations. 30

Figure 11. Validation of the satellite forecast on the Eye2sky domain. (01.07.2020 to 31.08.2020) 32

Figure 12. Validation of the satellite forecast on the Eye2sky domain using relative error metrics. (01.07.2020 to 31.08.2020) 33

Figure 13. Validation of the ASI network forecast on the Eye2sky domain (01.07.2020 to 31.08.2020). 34

Figure 14. Undefined values encountered on the ASI forecast domain for an extremely unfavorable case (low cloud height with strong winds). 34

Figure 15. Benchmark for the combined forecast on the nominal synchronization case. **Top:** Error metrics RMSE(o) and MAE(d). **Bottom:** average optimized combination weights(x) and optimized combination bias term (Δ) in the secondary axis. 35

Figure 16. Average RMSE of $k_{forec} *$ in terms of the variability index (VI) for $\Delta t = 5$ min and $N=25$ min(bin width = 0.02). The forecasts shown are ground persistence (·), satellite persistence (o), satellite (d), ASI network (□) and combination of satellite and ASI network (Δ). On the secondary axis the relative cumulative sum of the available points (+)..... 39

Figure 17. Difference of average RMSE $k_{forec} *$ with the average RMSE $k_{gnd} *$ in terms of the variability index using $\Delta t = 5$ min and $N=25$ min (bin width = 0.02). The forecasts shown are

ground persistence (\cdot), satellite persistence (\circ), satellite (\diamond), ASI network (\square) and combination of satellite and ASI network (Δ). On the secondary axis the relative cumulative sum of the available points (+) 40

Figure 18. Difference of average RMSE k_{forec} * with the average RMSE k_{gnd} * in terms of the variability index bins (bin width = 0.02) using N=25 min. Each figure represents a value of Δt from 0 to 8 min. The forecasts shown are ground persistence (\cdot), satellite persistence (\circ), satellite (\diamond), ASI network (\square) and combination of satellite and ASI network (Δ). On the secondary axis the relative cumulative sum of the available points (+) 41

Figure 19. Difference of average RMSE k_{forec} * with the average RMSE k_{gnd} * in terms of the variability index bins (bin width = 0.02) using N=25 min. Each figure represents a value of Δt from 9 to 17 min. The forecasts shown are ground persistence (\cdot), satellite persistence (\circ), satellite (\diamond), ASI network (\square) and combination of satellite and ASI network (Δ). On the secondary axis the relative cumulative sum of the available points (+) 42

Figure 20. Relative scatter density plot of the increments of the clear sky index of the forecast source Δk_{forec} * with the increments of the clear sky index of the ground measurements Δk_{gnd} * for $\Delta t = 5$ min (the colors are in logarithmic scale). 43

1 Introduction

1.1 Context

Solar power generation, based on Photovoltaic (PV) and Concentrated Solar Power (CSP), are fast growing technologies that have established themselves as an important contributor of the overall power energy generation sector. In 2020, the global production of PV power is estimated to be between 140 and 160 GW. In the same year the number of countries that have installed more than 1 GW PV power generation annually increased to 18 (Jäger-Waldau, 2021). This growth implies a constant increasing PV power generation penetration in several electric power systems around the world. As a result, the stability of the electrical grids is threatened due to the inherent weather dependent nature of this generation (mostly due to clouds formation and movement). The ability to forecast irradiance becomes then a crucial factor to ensure PV power reliability, optimal management strategies (e.g., storage) and grid stability.

During the last decades, several techniques have been developed for estimating the irradiance at the earth's surface. Due to their high spatial and temporal coverage satellite based forecasts and Numerical Weather Prediction models (NWP) are the most commonly used techniques for intraday irradiance/power forecasting (Hammer et al., 2003 / Sperati et al., 2016). This high coverage is achieved in detriment of a low temporal resolution, commonly 15 minutes to 1 hour, and a low spatial resolution, commonly in the kilometres range. More recently, short term forecasts (nowcast) from All Sky Imagers (ASI) provide highly resolved temporal and spatial irradiance predictions on a localized level. These nowcasts can reach a spatial resolution of down to 5 m × 5 m and with lead times up to 15 min (Nouri et al., 2020b). So far, ASI-based nowcasts have been applied mainly to predict the local production of solar power directly on the plants where they are located.

In this context, two main research questions are to be addressed within this work:

1. Does the combination of multiple ASIs installed on an extended network allow an effective increase of the spatial extent, forecast horizon and overall forecast accuracy?
2. Could we combine these forecast sources of such heterogeneous nature to produce temporally and spatially highly resolved unique forecasts that exploits the advantages of the individual sources?

1.2 Objectives

In this task we first aimed to develop new algorithms which allow to use the novel Eye2Sky all-sky-imager (ASI) network to provide spatially and temporally highly resolved nowcasts of solar irradiance for whole distribution grids. In particular, we aimed to generate nowcasts with a spatial resolution in the order of 10 m and a temporal resolution of 30 sec. Further, the nowcast should be applicable to the whole Eye2Sky network area with its extent of 100 km x 100 km. Finally, in the urban area of Oldenburg, located in the center of Eye2Sky network, we aimed to generate ASI-based nowcasts for forecast lead times of up to two hours. To achieve these goals, the new algorithms aim to combine the analysis products of the individual ASIs and ASI pairs to mitigate deviations, to increase the computational efficiency as well as spatial and temporal coverage of the ASI-based nowcast.

Our second aim in this task is to develop an algorithm for combining data from ASIs, satellite and NWP products in order to achieve a highly resolved hybrid irradiance forecast. This new combined forecast should present an enhanced update rate, higher temporal and spatial resolutions and an accuracy improvement with respect to the individual forecast inputs for horizons of up to 1 to 6 hours. The newly developed method should assimilate the higher

resolution camera information into the other forecasts cloud scenes to obtain an overall RMSE improvement over the whole forecast horizon. As a result, the combination should be able to provide minute-level variability information of the overall product. To develop this new algorithm, we have available the forecast for the ASI network for 2 consecutive summer months in the year 2020 (July and August 2020). In the same time range, the DLR's operational satellite forecast is also available. In the context of this project, our Partner Meteo France had processed the high-resolution NWP forecast AROME for 2 summer months on 2019 (July and August 2019) and 2 winter months of 2020 (February and March 2020). For the Arome's processed summer months it was not possible to process an accurate ASI network forecast due to the low number of cameras installed at the time. The winter months data are of low interest when developing an algorithm for solar irradiance forecast. Due to this, for the time being, the time range including the 2 summer months with Satellite and ASI network forecasts are used for this work. The NWP model Arome could not be taken into account on the developed combination.

1.3 Contributions

The enhanced ASI-based analysis and forecast products were developed as maps. These map products can be exported and can be combined easily with data from other sources. In particular the combination of such maps with satellite-based maps was already tested in this study. In the same way, this interface can be used to support the ASI-based nowcast with data from satellite or other sources. These analysis and forecast products were validated in comparison to data from state-of-the-art ASI-based approaches and were found to be notably more accurate. The analysis products include cloud base height, cloud motion vectors and cloud attenuation (individual for each grid cell of the map). The forecast products include maps of global horizontal, diffuse horizontal and direct normal irradiance.

The hybrid combined ASI network + satellite forecast developed in this study is produced as maps or time-series as needed. The input forecasts for the combination are needed as map products. The main regression algorithm used to produce the combined forecast is based on irradiance timeseries from the forecast input sources for pixels where ground measurements are known. Once the optimal combination factors are found, the hybrid forecast global irradiance maps or timeseries are produced. The highly resolved hybrid forecast was validated against the individual input sources and satellite persistence. This newly developed forecast outperforms the error metrics used on this study for all lead times processed.

2 Overview of the methodology

In this deliverable we worked mainly on the development of 2 new irradiance forecast methods, the ASI network forecast (part 1, described in Section 3) and a hybrid satellite + ASI network combined forecast (part 2, described in Section 4). Figure 1 shows the data flow between the different stages of development. Both forecast methods used reference data from the project's **dataset # 1**, defined in the Smart4RES Data Management Plan as the “**NorthWest meteorological measurement network & PV plants**”. This dataset is based on the meteorological and ASI camera stations installed in the **Eye2sky network** in Northwest Germany (see Figure 2).

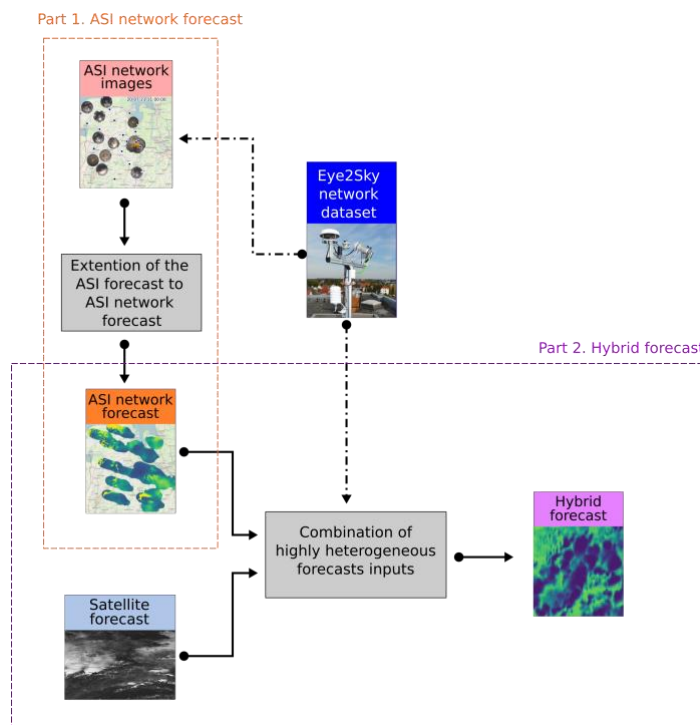


Figure 1. Overview of the data flow between the different parts of this deliverable

In the first part of this study, we have developed a method to produce irradiance forecasts from a highly dense network of ASIs (29 in 100 km²). The ASIs on this network are used to derive a segmented cloud mask, the cloud heights and cloud speeds. Here, 3 cloud mask images are used to derive the cloud motion vectors. These vectors are used to extrapolate the cloud mask into the future. Finally, ground observations from the same dataset are overlaid on the cloud masks to derive irradiance maps. An intelligent combination of the high spatial density of ASIs allows to extend the spatial and temporal coverage compared to a single (or pair) ASI system.

In the second part of this study, we developed a method to combine this newly developed ASI network forecasts with the well-known satellite-based forecast. These 2 forecast inputs are highly heterogeneous in nature. Therefore, first the forecasts inputs are homogenized in space and time. Then, historical forecasts are used to optimize the coefficients on the linear combination of the forecast inputs. Once the optimized coefficients are found, the present (and not historical) forecasts are combined using the optimized weights to produce a hybrid irradiance forecast in the form of maps or timeseries. At the end the hybrid forecast shows improved error metrics compared to the forecast inputs for a horizon of 30 minutes and for conditions with high irradiance variability.

3 Advanced analysis of camera images for cloud characterization

3.1 Introduction

In the first part of this study, we developed the enhanced ASI-based nowcasting system which aims to provide nowcasts for higher lead times and to increase the accuracy of the nowcast in comparison to previous ASI-based nowcasts.

Errors in the estimation of cloud base height (CBH) are expected to strongly affect a nowcast's accuracy (Nouri et al., 2019a; Kuhn et al., 2019) as the position of the shadow cast on the ground by a specific cloud is directly related to the sun elevation angle and CBH. We start from the estimations of CBH from individual ASI pairs. A statistics-based approach then merges these CBH values into a more accurate estimation.

In order to detect small scale variations of the solar irradiance, the location and attenuation of clouds need to be captured more accurately. A cloud classification is used as indicator of cloud attenuation. The indicator of cloud attenuation received from multiple ASIs is combined to filter out erroneous observations of clouds or sky.

Spatial variations of diffuse horizontal irradiance (DHI) were typically neglected by previous ASI-based systems (e.g. Nouri et al., 2021). A new method is developed which measures DHI by the distributed ASIs. Consecutively, these measurements are combined into a map of DHI.

To forecast the positions of clouds over larger lead times, a more accurate cloud tracking procedure is required. For this purpose, the cloud motion vectors from all ASIs are combined into a more accurate estimate. Further, the new cloud tracking procedure also accounts for changes of the cloud speed and direction of motion over the trajectory of a cloud particle.

3.2 Case studies

The development and validation of the ASI-network nowcast is performed with the **dataset # 1**, defined in Smart4RES Data Management Plan as the "**NorthWest meteorological measurement network & PV plants**". This dataset is based on the measurements from the DLR's Eye2Sky network, shown in Figure 2. The dataset is summarized in Table 1.

	ASI network	ASI network increased lead times
Spatial resolution	50 m	50 m
Extent	40km x 40 km (centred in Oldenburg city)	120 km x 120 km (Eye2Sky region)
Product projection	Transverse mercator	Transverse mercator
Number of ASIs included	12	23
Forecasts update	30 s	30 s
Forecast step	1 min	5 min
Forecast horizon	30 min	130 min
Availability	120 days in 2020	25 days in 2020
Parameter	GHI	GHI
Type	Deterministic	Deterministic
Provider	DLR	DLR

Table 1. Dataset used for the development and validation of the ASI network.

Eye2Sky - Cloud camera and meteorological measurement network in Oldenburg

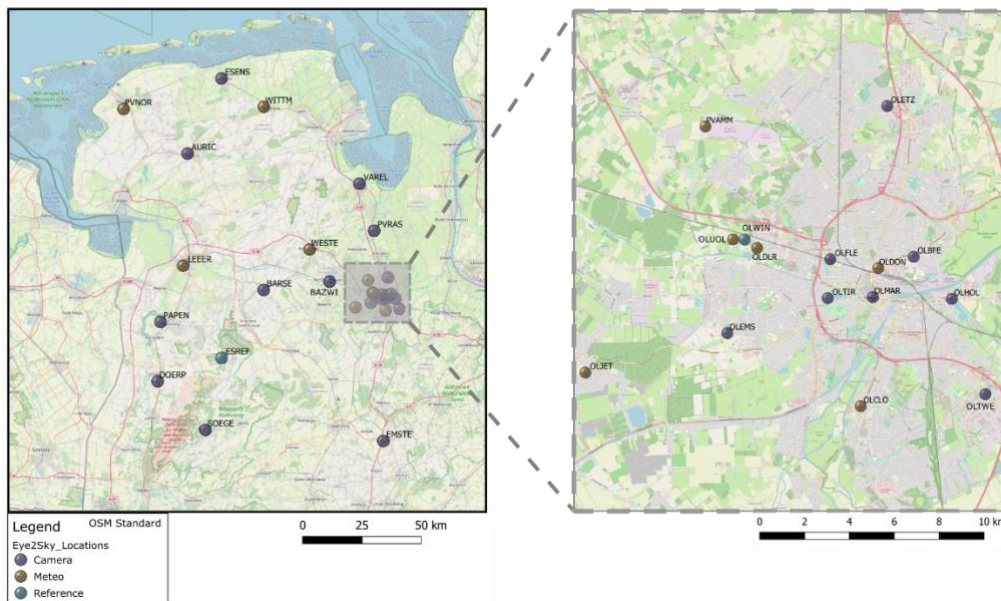


Figure 2. Eye2sky Network overview. **Camera** stations (blue circles) are camera only stations, **Meteo** stations (brown circles) are camera + meteorological stations equipped with an RSI and **Reference** (green circles) are only meteorological stations equipped with thermal radiometers + solar tracker.

As reference ground data three meteorological stations from the Eye2sky network are taken: **OLDON**, **OLCLO**, **OLUOL**. These are the reference stations available inside the extent of the ASI network forecast. Each of these meteorological stations is equipped with a rotating shadowband irradiometer (RSI) to measure DNI, DHI and GHI. The description of the ground validation dataset is shown in Table 2. The days used for model development and validation were selected to represent the year 2020 in terms of seasons and of meteorological conditions expressed by the DNI variability classes of Schroedter-Homscheidt et al. (2018). Further, the days in the validation dataset were chosen to form series of typically 3 to 4 days. This rule was not followed strictly due to data gaps as well as to represent the meteorological conditions of the year 2020 as good as possible.

Data type	Parameter	Locations	Days from 2020	Duration	filtering
Training	DNI, DHI	OLDON	January 13, 24; February 04, 15, 26; March 08, 13, 19; April 10, 21; May 13, 24; June 03, 15, 26, July 07, 18, 29; August 07, 09, 20, 31; September 11, 22; October 03, 13, 25; November 05, 16, 27.	30 days	Solar elevation > 15°
Validation	GHI	OLDON, OLUOL, OLCLO	January 14, 15, 16, 17, 25, 26, 27, 28; February 05, 06, 07, 08, 16, 17, 18, 19, 27, 28, 29; March 09, 10, 11, 14, 15, 16, 20, 21, 22; April 11, 12, 13, 15, 17, 18, 19, 24; May 15, 16, 25, 26, 27; June 05, 06, 07, 16, 17, 18, 27, 28, 29; July: 08, 09, 10, 11, 19, 20, 21, 22, 30, 31; August 01, 02, 08, 10, 11, 12, 13, 21, 22, 23, 24; September 01, 02, 03, 04, 12, 13, 14, 15, 23, 24, 25, 26; October 04, 05, 06, 15, 16, 17, 26, 27, 28.	92 days	Solar elevation > 15°
Validation increased lead times	GHI	OLDON	January 17; February 05, 07, 17, 18; May 15, 16, 26; June 05, 18, 28, 29; July 10, 11, 30; August 02, 12, 21; September 01, 04, 12, 13, 25; October 17, 28	25 days	Solar elevation > 15°

Table 2. Datasets used for the development and for the validation of the nowcast.

3.3 Methodology

3.3.1 Estimating cloud height

Nowcasting systems based on all-sky-imagers (ASIs) need to know CBH accurately to nowcast the spatial distribution of solar irradiance around the ASI's location. Two ASIs located at a distance of usually less than 6 km can be combined into an ASI-pair to measure CBH. However, the accuracy of such systems is limited. For this reason, we developed a method to estimate CBH more accurately by the ASI network. The deviations of 42 ASI-pairs located in the urban area of Oldenburg were studied in comparison to a ceilometer and characterized by camera distance.

The ASI-pairs were formed from seven ASIs and feature camera distances of 0.8 to 5.7 km. Each of the 21 tuples of two ASIs, formed from seven ASIs, yields two independent ASI-pairs. For this purpose, the ASIs used as main and auxiliary camera respectively are swapped. The deviations which were found for the ASI pairs were compiled into conditional probabilities telling how probable it is to receive a certain reading of CBH from an ASI-pair given that true CBH takes on some specific value. Based on such statistical knowledge, in the inference, the likeliest actual CBH is estimated from the readings of all 42 ASI-pairs.

ASI-pairs with small camera distance (especially if < 1.2 km) are found to be accurate for low clouds (CBH < 4 km). In contrast, ASI-pairs with camera distance of more than 3 km provide smaller deviations for greater CBH. No ASI-pair provides most accurate measurements under all conditions. Overall, the ASI network, which uses ASIs at different distances, provides combined measurements of CBH which are more accurate than any of the tested ASI-pairs alone. The method and validation summarized at this point is described in more detail in Blum et al. (2021).

3.3.2 Identifying the spatial distribution of cloud attenuation

In this section the ASI network's procedure to determine the locations of clouds including their height and shape and to assign attenuation to these is described. Such cloud modeling is a central subtask in ASI-based nowcasting, in particular if solar irradiance should be predicted not only for an ASI's location but spatially resolved. In comparison to previous ASI-based approaches to predict maps of solar irradiance, typically relying on not more than four ASIs located in proximity, an ASI network can be expected to increase the accuracy of cloud modeling as multiple perspectives on clouds are combined. Previous operational ASI-based nowcasting methods (Peng et al., 2015; Nouri et al., 2018) provide a useful and practically proofed basis for the present procedure. However, these procedures were not suited yet to combine the observations, i.e., maps of cloud parameters, received from very different perspectives and with different accuracies. To solve this, a new method was developed.

As a starting point, sky images are segmented, undistorted, georeferenced and transformed into maps of an attenuation index. The attenuation index is introduced as a parameter which indicates the presence and the expected attenuation of a cloud for each grid cell. As shown in Table 3,

Cloud class	Attenuation index AI
undefined	n.d.
low layer/ thick cloud	1
mid layer cloud	0.7
high layer/ thin cloud	0.2
clear sky	0

Table 3. Five cloud classes received from cloud segmentation are mapped to values of the attenuation index AI

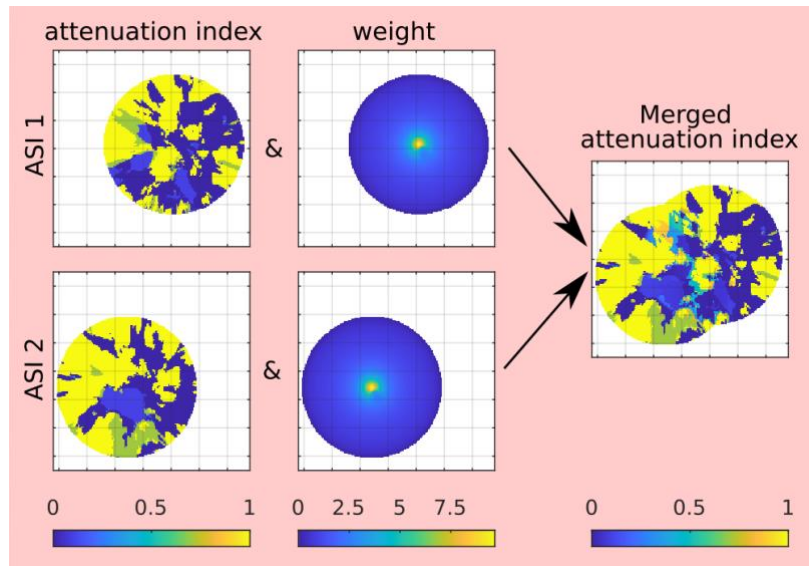


Figure 3. The accuracy-weighted merging procedure is shown exemplarily with only two ASIs for 05 June 2020, 10:22:00. Each ASI delivers a georeferenced map of attenuation index AI_i (left column); the map of AI from each ASI is weighted by u_i^{-1} (center column), the inverse of the expected local uncertainty of AI; the weighted average based on $AI_i u_i^{-1}$ from all included ASIs yields the merged map of AI.

cloud classes are provided by the segmentation procedure (Fabel et al., 2022) for each image pixel of an individual ASI. These five cloud classes are mapped to one of five values of attenuation index which range between zero and one. The maps of the attenuation index received from multiple ASIs are then combined to receive a more accurate map of the attenuation index.

From the principles of error propagation, it is expected that multiple observations, i.e., maps of cloud properties, merged by accuracy-based averaging are significantly more accurate than the most accurate of those observations alone. Based on these considerations, ASIs are placed at distinct points in and around Oldenburg and are included in the dedicated merging procedure as follows. First, the sources of uncertainty in the maps of the attenuation index are determined. As sources of uncertainty, perspective errors and segmentation errors are considered. Further, a base uncertainty is included which accounts for other less dominant sources of errors. Based on the local uncertainty of the single ASIs' maps of the attenuation index, the merging procedure assigns a weight to the grid cell of each map and averages the weighted maps as summarized in Figure 3. This merging procedure can be adapted for various parameters related to clouds such as cloud velocity, DHI and attenuation index.

Consecutively, a statistical procedure is applied to self-calibrate the relationship between the merged map of attenuation index and cloud attenuation. For this purpose, from the DNI measurement of RSI station DON and by an estimation of clear sky DNI, cloud attenuation is determined.

Both steps were developed also to incorporate a sky-image-based classification of cloud types more adequately than done by previous methods. By this, cloud attenuation is modeled with a finer graduation.

3.3.3 Spatial variability of diffuse irradiance

In ASI-based nowcasting systems diffuse horizontal irradiance (DHI) is frequently measured in a single point by a measurement instrument such as a sun tracker or a rotating shadowband irradiator which supports the nowcast. DHI is then assumed to be spatially homogeneous and persistent over the forecasted lead times (e.g. Nouri et al., 2020b). This simplification can induce errors to the nowcast. Additionally, such measurement instruments increase the costs of nowcasting systems. To avoid these shortcomings, we developed a procedure which measures DHI based on the image of an

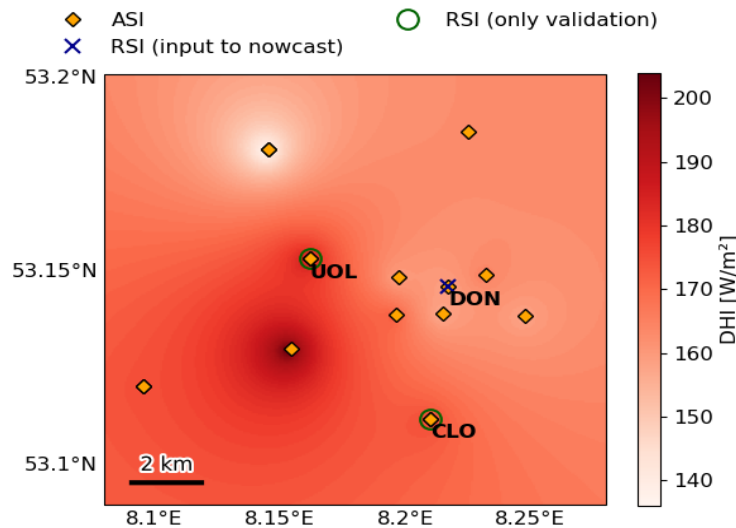


Figure 4. An exemplary map of DHI in the urban area of Oldenburg on 10 July 2020 13:00:00 (UTC) is shown. RSI station DON (x) and all ASIs in the urban area (◊) provide a measurement of DHI to the nowcast. The RSIs at UOL and CLO (◊) are used as references for the validation.

all-sky imager and an external source of global horizontal irradiance (GHI) or direct normal irradiance (DNI). GHI can for example be received from a regular thermopile pyranometer. This measurement technique was developed and validated at two sites in Spain and Germany. Our results indicate that the measurement technique can be applied at both sites. DHI is measured significantly more accurately than reported in previous works using an ASI alone for the measurement of DHI. This method and the validation are described in more detail in Blum et al. (2022).

The ASI-based measurement of DHI is applied to every ASI in Eye2Sky. This measurement is available at each of the numerous ASI stations. The inclusion of all ASI stations instead of only the meteorological stations in the analysis of DHI increased the number of locations in which DHI was available from 3 to 12 in the urban area of Oldenburg and from 7 to 23 in the whole area of Eye2Sky, at the time of the experiments. While the number of stations will increase in the future, the ratio of meteorological stations and regular ASI stations will remain similar. During nowcasting, the DNI used in the correction of the ASI-based measurement is received from the analysis of DNI.

By the procedure described in Section 3.3.2, point-wise measurements are merged into a map which covers the area of Eye2Sky. Both, ASIs and RSIs, can provide point-wise measurements of DHI. In this study, only the RSI at DON is included in the nowcast. All other RSIs are excluded from the nowcast and used only for validations. For this study it was necessary to reserve radiometers which are only used for validations. However, in the future, the nowcast accuracy

of DHI and also DNI and GHI can be improved if all radiometers of Eye2Sky are included in the calibration of the ASI-based measurement of DHI and also in the nowcast. Further, each ASI station could be equipped with a thermopile pyranometer adding only moderate costs. We expect that this enhancement would allow to nowcast maps of DHI and GHI at highest accuracy. Figure 4 shows an exemplary DHI map for the urban area of Oldenburg. Notable variations of DHI are visible in this map which could not be resolved by a single measurement of DHI or by the state-of-the-art ASI pair. The quality of the ASI-based measurement of DHI is not expected to reduce significantly at an increased distance between the respective ASI and RSI station DON. The newly developed ASI-based prediction of DHI will therefore be even more advantageous at larger distances from the urban center, i.e., in the rural area of Eye2Sky.

3.3.4 Estimating cloud velocity and tracking clouds

The individual ASIs included in the ASI network determine the angular cloud velocities in eastern and northern direction by the procedure of Nouri et al., 2019a. Each individual ASI delivers an orthoimage of the angular cloud velocities consisting of 3×3 zones. For each zone and both directions, an average angular velocity is provided. Using the local CBH, each orthoimage of the angular velocity is converted into a map of cloud velocity. The angular velocity in each grid cell of the ASI-based orthoimage is mapped to the grid cells of a georeferenced map. The angular cloud velocity in each grid cell of the map is then translated into the absolute cloud velocity by the relationship used by Wang, Kurtz, and Kleissl, 2016. The maps of cloud velocity from all ASIs are merged into a single map by the merging procedure developed in Section 3.3.2. However, the uncertainty terms are different in this case. By these steps, one map of cloud velocity is determined for the cloud velocity in eastern and one for the cloud velocity in northern direction. In the georeferenced maps, each grid cell has a size of $50 \text{ m} \times 50 \text{ m}$.

With the large number of included ASIs, in large parts of the urban area, cloud velocities from multiple ASIs are merged. This is expected to reduce the uncertainty of the cloud velocity information. Additionally, the merged map of cloud velocity covers a larger area compared to a single ASI or an ASI pair. The merged map of cloud velocity can still exhibit gaps for which no data are available. These gaps are filled by inward interpolation assuming that cloud velocity is smooth within these zones.

The maps of cloud velocity cover the whole nowcasted area. We then follow the concept, that every particle of a cloud is transported by the velocity field which is described by the maps of cloud velocity. This concept is seen as a refinement of previous approaches (e.g., Nouri et al., 2019a), which determined a single velocity for each cloud and set it constant for all forecasted lead times. In the present model, particles within a single cloud can have different velocities. This can cause clouds to unite, to decompose or to change their shape. Additionally, cloud particles can change their speed and direction of motion over the forecasted lead times even though the maps of cloud velocity are static in our model. The tracking procedure can be applied to any parameter which is given as map and which is expected to move along the clouds' velocity field. In the present nowcasting procedure, these tracked parameters are DHI and cloud attenuation.

3.4 Results and Discussion

3.4.1 Benchmarking the overall performance

In the first step, the ASI network's overall performance for GHI nowcasting is assessed. ASI pair DON-FLE and persistence based on RSI station DON are used as reference nowcasts in the benchmark.

The deviations metrics RMSD, MAD and bias are used to summarize the nowcasting approaches' uncertainty for GHI nowcasting at the sites DON, UOL, CLO. This is shown in Figure 5. At all reference stations, the ASI network delivers clearly more accurate nowcasts of GHI, in terms of RMSD and MAD, compared to both the ASI pair DON-FLE and persistence. This finding holds for all forecast lead times at the stations UOL and CLO and for all lead times greater than 1 min at DON. Depending on the evaluated station, the ASI network reduces RMSD by 23-30% ($35 - 50 W/m^2$), 15-21% ($25 - 37 W/m^2$), 12-16% ($20-27 W/m^2$), 8-12% ($14 - 21 W/m^2$) over persistence at evaluated lead times of 5, 10, 15, 20 min. The ASI pair's advantage over persistence in terms of RMSD and MAD depends strongly on the evaluated location and forecast lead time. At lead times of more than 5 - 17 min, depending on the location and metric, the ASI pair does not reduce the deviations over persistence. Additionally, the ASI pair's RMSD and MAD are comparably large at CLO which is located roughly 3.8 km to the south of the two ASIs. These effects are explained by the limited field of view of the ASI pair's ASIs. Frequently, the ASI pair's field of view is too small to observe the clouds at forecast instance time (i.e. at the timestamp based on which the forecast is created) which are at the evaluated location at the forecasted time. In these cases, the ASI pair uses an auxiliary technique which is comparable to persistence. In comparison, the ASI network's advantage over the ASI pair and persistence reduces only moderately for lead times up to 15 min. This is reasonable due to the ASI network's increased spatial coverage.

As to be expected for a sufficiently large data set, persistence has a bias close to zero at all sites and for all lead times. The ASI pair performs in general as expected from prior validations (see e.g., Nouri et al. 2021, non-hybrid ASI-based nowcast). For the overall data set with its challenging atmospheric conditions and typically rather low sun elevations, a certain small advantage over persistence is found in terms of RMSD and MAD. The conditions under which also the ASI pair has a clearer advantage over persistence are analyzed in more detail in Section 3.4.2.

The ASI network performs similar in the central location DON and in the peripheral locations, UOL and CLO. Only, at lead times of up to 3 min, RMSD and MAD at UOL and CLO are much larger than at DON. This effect is mostly explained as RSI DON is used to estimate local cloud attenuation. This causes a local correction of the nowcast at DON. At lead times of more than 3 min, the RMSD shows a similar behavior at all sites. After the first minutes, those local adaptations can be expected to be of smaller relevance. Still, the area around DON is monitored by the largest number of ASIs. Therefore, most accurate nowcasts are received in the center of the ASI network. On the other hand, the deviations of the ASI network's nowcast are only moderately larger at UOL and CLO compared to DON. This supports the assumption that the ASI network's cloud modelling and DHI modelling procedures are suited to represent the whole urban area. So far, only a single ground-based measurement is included in the nowcast. This way, a sufficient number of meteorological stations was reserved for validations only. For applications, the measurements from all radiometers and possibly also from distributed PV installations can be included to adapt the local nowcast of GHI. This will clearly improve the ASI network's accuracy in these locations, making them comparable to DON.

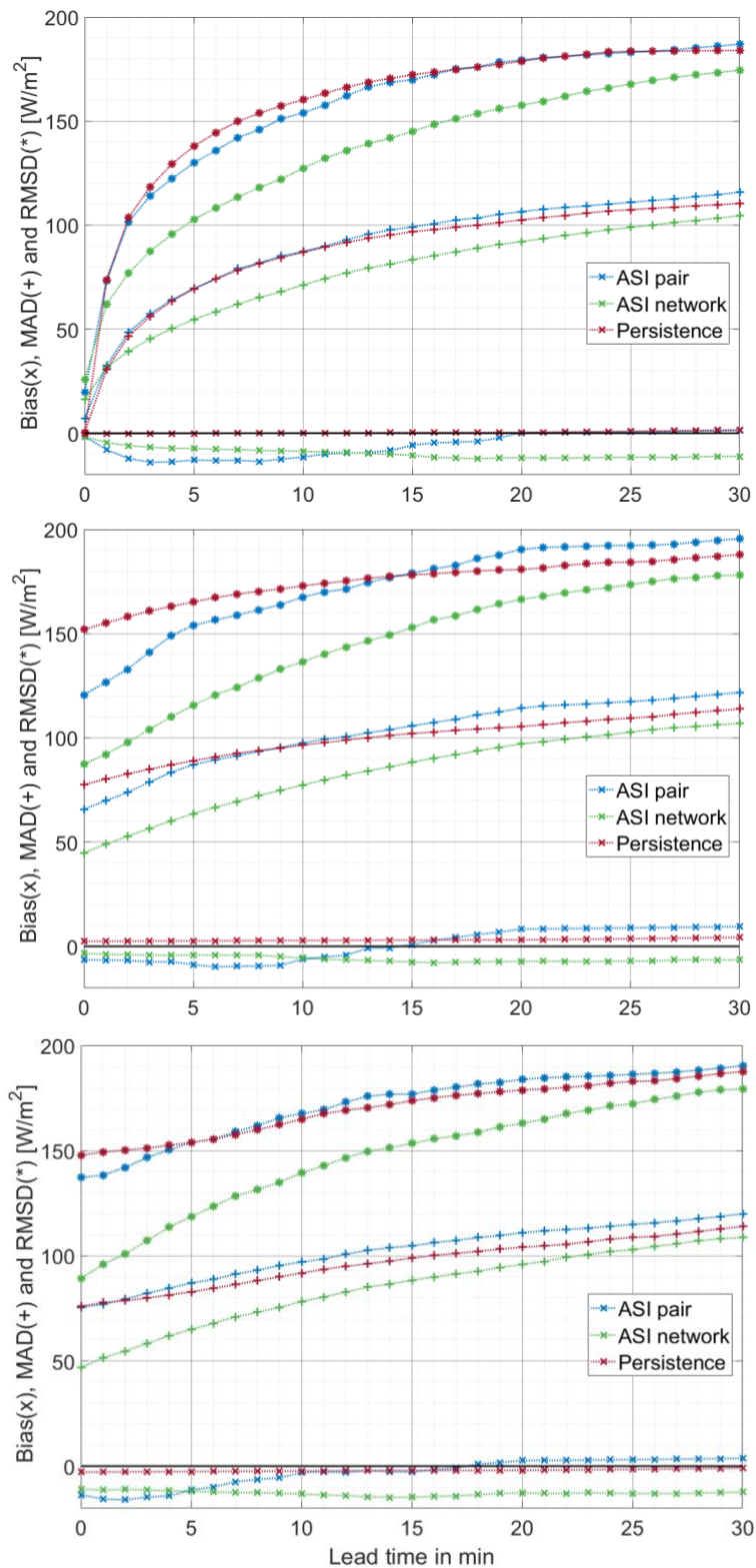


Figure 5. Deviations of the ASI-network-, ASI-pair- and persistence-based nowcasts of GHI for the locations DON (top), UOL (middle) and CLO (bottom) are evaluated over the 92-days validation dataset and are characterized by the metrics RMSD, MAD and bias.

3.4.2 Investigating the influence of DNI variability on nowcasting performance

Deviation metrics can vary strongly depending on the local climate. The influence of these conditions on the nowcast errors of ASI pair and ASI network is analysed in the following. This section investigates the narrowcast' RMSDs separately for eight DNI variability classes. These classes represent distinct meteorological conditions regarding DNI variability and also regarding the typical cloud coverage.

The 92-days test set is now divided into the eight DNI variability classes. The classification was already used in prior validations of the ASI pair (Nouri et al., 2020b; Nouri et al., 2019c). The meaning of the variability classes is summarized in Table 4.

All nowcasts, which are created based on a certain forecast instance time, are classified based on the DNI measurements of RSI DON within the 15 min which precede that forecast instance time.

Variability class	Sky conditions	DNI clear sky index	Variability
1	mostly clear sky	very high	low
2	almost clear sky	high	low
3	almost clear sky	high/ intermediate	intermediate
4	partly cloudy	intermediate	high
5	partly cloudy	intermediate	intermediate
6	partly cloudy	intermediate/ low	high
7	almost overcast	low	intermediate
8	mostly overcast	very low	low

Table 4. This table summarizes the sky conditions indicated by each of the eight DNI variability classes according to Nouri et. al. 2021.

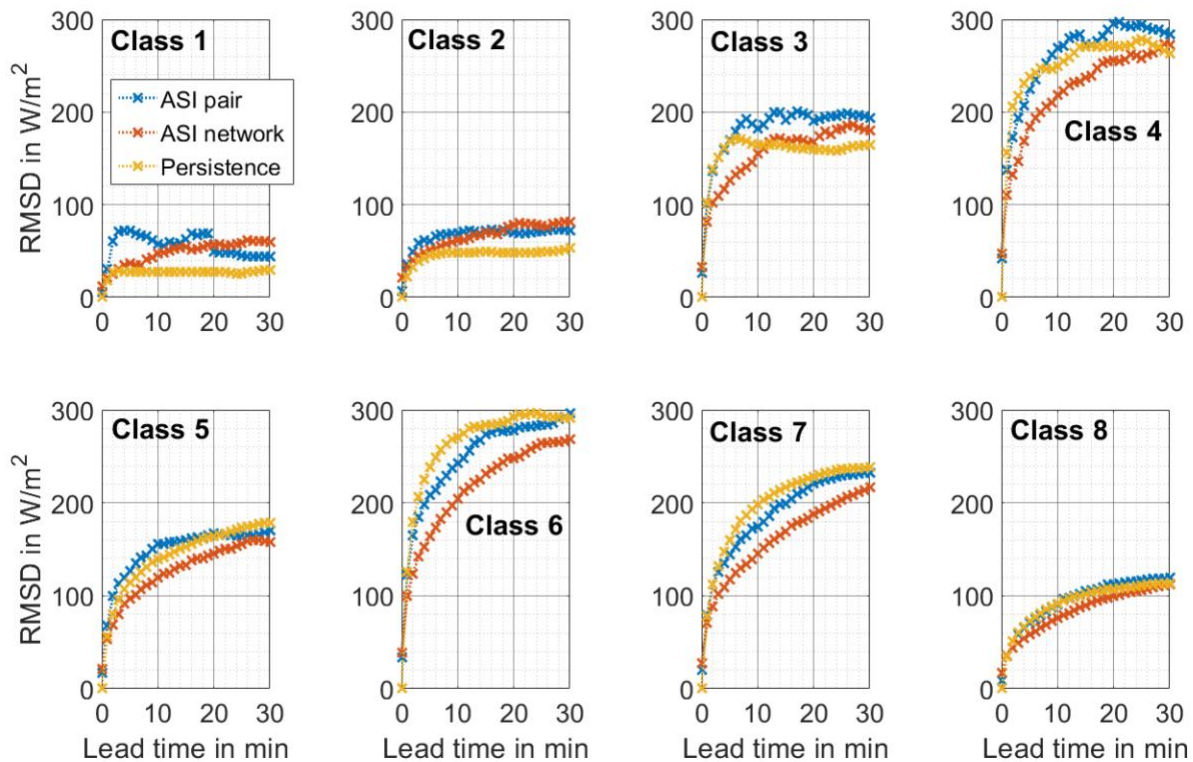


Figure 6. The RMSD of the ASI-pair- and ASI-network-based GHI nowcast for DON is plotted over the lead time for each of the eight DNI variability classes. The present DNI variability class is determined from the DNI measured by RSI DON in the 15 min preceding the respective forecast instance time.

Figure 6 shows the corresponding evaluation for DON. Qualitatively, the ASI pair's performance at DON matches the one found by Nouri et al. (2021) for the same system (non-hybrid ASI-based nowcast) at a different site. In particular, the performance of the ASI pair in relation to the performance of persistence is reproduced for the largest part.

In the classes 3 – 8, the ASI network's nowcast for DON outperforms the ASI pair clearly. Only in the variability classes 1 and 2 the ASI network's advantage is smaller. Variability classes 1 and 2 represent conditions with clear sky and sporadic optically thin clouds. In these classes, at lead times greater than 15 min, both approaches perform similar. The ASI network outperforms persistence clearly in most classes and at most lead times. The ASI network has the largest advantage (by up to 36% and up to 75 W/m^2) over persistence in the most variable classes 4, 6 and 7, in which persistence yields large errors. Both ASI-based approaches are outperformed by persistence for variability classes 1, 2. This effect was to be expected as the persistence nowcast is well suited for steady conditions. Still, in classes 1 and 2, the magnitude of the RMSD is comparably small for all tested approaches. Besides DON, the nowcasts' RMSDs were also evaluated at station UOL. UOL with its comparably large distance of 3.8 km from RSI station DON represents the periphery of the urban area. Qualitatively, the evaluation for UOL showed the same effects as the one for DON. In most classes, the ASI network's advantage was even more pronounced compared to DON.

In summary, this evaluation indicates that the ASI network reduces the nowcast's RMSD compared to the ASI pair and compared to persistence in classes 3-8. Only in classes 1 and 2 ASI pair and ASI network perform similarly. In these classes, the ASI network's RMSD is up to 35

W/m² larger than the one of persistence while the RMSD values of all nowcasts are comparably small in these classes.

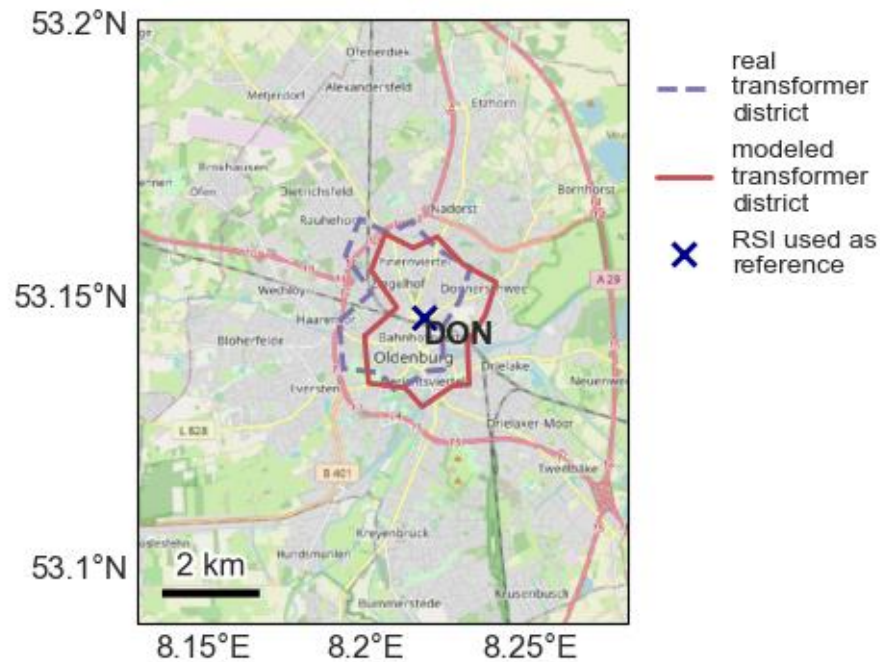


Figure 7. This map shows the transformer district (orange solid shape) for which average GHI is nowcasted in Section 3.4.3. RSI DON (X) provides the reference measurements. The modeled transformer district is imaginary but has the same shape as a real transformer district in the center of Oldenburg (blue dashed shape). (background © [OpenStreetMap](https://openstreetmap.org/) contributors 2022. Distributed under a Creative Commons BY-SA License.)

3.4.3 Nowcasting errors at increased lead times

In the following, the errors of the ASI network's nowcast at higher lead times of up to 130 min are investigated. In particular, this section examines the ASI network's advantage over persistence. In the year 2020, in which the experimental data was acquired, a maximum of ten ASIs from the rural area was available for nowcasting. This leads to the following restrictions for the present evaluation. Increased lead times of e.g., one hour can only be forecasted under certain conditions with cloud motion from certain western directions. Also in these cases, the nowcast is frequently only available for specific lead times as the clouds need a specific time, which depends on their speed, in which they are transported from the point of observation to the urban area. For this evaluation, a subset of the 92-days-validation data set (see Section 3.2) is used. This subset contains 25 days on which clouds move in the specific directions for which high forecast lead times can be covered in theory. As before, timestamps are only evaluated, if the ASI network provides a valid nowcast for them.

In the evaluations up to this point, it has become visible that variations of GHI are nowcasted less accurately at higher lead times. Therefore, this section intends to validate aggregated GHI which is relevant in a distribution grid application and is less prone to that source of error. From the ASI network, I therefore evaluate nowcasted GHI averaged over the transformer district shown in Figure 7 (orange solid shape) and over a time span of 5 min. 5-min-average GHI measured by RSI DON (blue cross) is used as reference.

RSI DON is located in the center of this transformer district. A similar validation approach is often used for satellite-based or NWP forecasts. A persistence nowcast using the measurements of RSI DON serves as benchmark. The modeled transformer district is only imaginary. It has the

same shape as a real transformer district located in the center of Oldenburg (blue dashed shape in Figure 7). The transformer district was shifted for this evaluation so that its geometric center coincides with the location of RSI DON. No actual aggregated GHI or PV production data are available for this validation. Therefore, this shift aims to increase the comparability of nowcast and reference measurement.

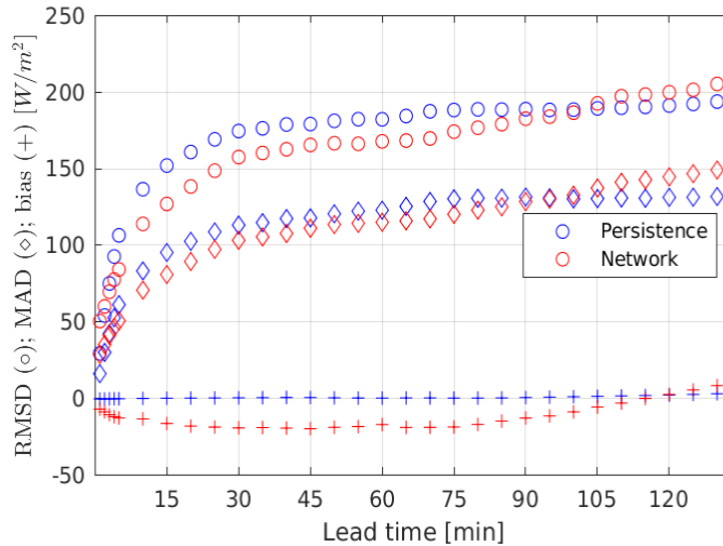


Figure 8. Deviation metrics RMSE (◊), MAD (◊) and bias (+) are plotted for the persistence nowcast (blue) and for the ASI network nowcast (red). Unlike Figure 5, this evaluation is restricted to 25 days but covers lead times of up to 130 min. The deviation metrics evaluate 5-min average GHI from RSI DON and 5-min average GHI aggregated over the area of the transformer district shown in Figure 7.

Figure 8 summarizes the resulting deviation metrics over the lead time. The ASI network outperforms persistence in terms of MAD and RMSE at lead times of 3 min to 95 min. In this range of lead times, the ASI network reduces the RMSE by up to 21% and up to 25 W/m^2 over persistence. As to be expected, persistence yields a negligible bias. The ASI network's nowcast has a moderate negative bias with a magnitude of less than 20 W/m^2 .

This validation indicates a certain advantage of the ASI network over persistence. Further, the validation may overestimate the deviations of the ASI network's nowcast. The nowcast provides spatially averaged irradiance, whereas only a pointwise measurement is available as reference for the validation. To some extent, this difference in the definition of the compared parameters can explain the deviations which were found.

4 Highly resolved combined ASI network, satellite forecast and NWP forecast

4.1 Motivation

A typical urban distribution has an extent around 100 km². Inside such an area, multiple photovoltaic (PV) roof size systems (of around 20kW) and occasionally also mid-range size systems (~MW) can be found. The accumulation of these type of systems in such a relatively small grid poses a threat to the grid's stability, mainly due to the intermittent nature of the power generation. To ensure grid stability, an accurate intra-day PV power forecast is needed. At the same time, accurate short term PV power forecasts are vital for the stakeholders that bid on electricity markets.

Nowadays, PV power forecasts are usually estimated using satellite and/or NWP irradiance forecasts. These forecast sources present the advantage of a high spatial and temporal coverage with the detriment of low temporal and spatial resolution. By the contrary, the newly developed ASI network forecast (see Section 3) is able to predict highly resolved irradiance forecasts on a local domain that matches quite well the typical distribution grid extent. At this scale, we are interested on finding a method to combine these highly heterogeneous forecast sources into a single hybrid forecast. The main idea is to assimilate the most relevant information of each source to produce a forecast with an increased accuracy metrics for the lowest temporal and spatial resolutions available.

4.2 Case studies

In order to produce and benchmark the newly developed combined forecast, we will use the following forecast sources in this study:

- **DLR VE's operational satellite based forecast (sat):** This method uses the raw images from a satellite (Meteosat Second Generation or MSG) to generate a Cloud Index (CI) image using the methods developed in (Hammer et al., 2015a), (Hammer et al., 2015b) and (Eumetsat, 2012). Using 2 consecutive CI images, Cloud Motion Vectors (CMVs) are calculated and used to extrapolate the CI into the future. This forecasted CI images are then used to calculate the irradiance value for every pixel. This is done by multiplying the forecasted CI values with irradiances derived from the Dumortier clearsky model (Dumortier, 1995) using the climatological turbidity values from (Remund., 2009). As the satellite takes one images every 15 min, the forecast has an update frequency and a forecast resolution of 15 min.
- **ASI network forecast (ASInet):** This forecast was developed on the DLR's Eye2Sky network (see Section 3.3) and it is fully described in the Section 3.3 In essence, the ASIs on this network are used to derive a segmented cloud mask, the cloud height and cloud speed. Then the cloud mask images are used to derive the CMVs, which are then used to extrapolate the cloud mask into the future. Finally, ground observations are overlaid on the cloud masks to derive irradiance maps. An intelligent combination of the high spatial density of ASIs (29 in 100k m² area) allows to extend the spatial and temporal coverage compared to a single ASI system. The ASIs on the network produce images every 30s. This allows the forecast to have an update of 30s using a forecast resolution of 1 minute. The forecast horizon varies depending on the position of the pixel, cloud height and the wind conditions. It ranges from 10 min to 60 min.
- **Satellite + ASI network combination (sat+ASInet):** In this study the we have developed a method to combine these highly heterogeneous forecast inputs. This is done to

improve the performance by taking advantage of the strengths of the individual forecasts. In essence, the forecast inputs are first homogenized in space and time. Then, historical forecasts are used to optimized the coefficients on the linear combination of the forecast inputs. Once the optimized coefficients are found, the actual forecasts (present) are combined using the optimized weights. The temporal resolution of the combined forecast is 1 min and the forecast horizon is 30 min. This method is explained in detail in Section 0.

- **Satellite Persistence (sat_persis):** This forecast is also based on the Heliosat 3 method. The difference to the satellite forecast is that the extrapolation is done using CMVs that are equal to 0. That is, as if the clouds did not move in time (note that the sun position does move in time). This forecast is used as baseline to be compared to the other forecast inputs as all forecasts should improve the long term performance over persistence. The temporal resolution and horizon of the forecast are the same as for the satellite forecast equal to 15 min.

The data available for the forecast combination is described on Table 5.

Parameter	Satellite	ASI network	High res. Arome NWP
Spatial resolution	1 km	50 m	1 km
Extent	Satellite view	40 km x 40 km (centred in Oldenburg city)	Central Europe
Product projection	geostationary	Transverse mercator	Plate Carree
Forecasts update	15 min	30 s	15 min
Forecast step	15 min	1 min	5 min
Forecast horizon	8 h	30 min	51 h (from run at 21:00)
Availability	Operational since begin 2020	01.07.2020 - 31.08.2020	01.02.2020 - 31.03.2020
Parameter	GHI	GHI	DSSR
Type	Deterministic	Deterministic	Probabilistic (25 members)
Provider	DLR	DLR	Meteofrance

Table 5. Available forecasts

The satellite forecast has been operational at DLR since the beginning of 2020, so there is no limit on its data availability. Having in mind solar power interests, the runs for the ASI network forecasts were processed on the DLR cluster for a range of 2 months in summer 2020 (July and August 2020). From the Arome model, the processing of the high-resolution NWP forecast was done for 2 summer months of 2019 (July and August 2019) and 2 winter months of 2020 (February and March 2020). For the Arome's processed summer months (July and August 2019) it was not possible to process an accurate ASI network forecast due to the low number of cameras installed at the time. The Arome's winter months data are of low interest when developing an algorithm for solar irradiance forecast. A new run of the Arome model for the months July and August 2020 is not possible due to the hardware (full daily run \approx 12 TB of storage) and personal resources needed for such a task. In this context, and having in mind the solar power application, we have decided to work with the summer months of 2020 using Satellite and ASI network forecasts. From the available data, this combination is a more sensible choice as it involves, at the same time, the high spatio-temporal resolution localized data (ASI), the averaged hourly information on the region (SAT) and high irradiance months (summer).

Accordingly, for the time being, the Arome NWP model could not be taken into account on the developed combination.

The evaluation of the chosen combined irradiance forecast sources is performed with the **dataset # 1**, defined in the Smart4RES Data Management Plan as the “**NorthWest meteorological measurement network & PV plants**”. This dataset is based on the measurements from the DLR’s Eye2Sky network, shown in Figure 2.

As reference ground data 4 meteorological stations from the Eye2sky network are taken: **OLDON, OLCLO, OLUOL, PVAMM**. These are the reference stations available inside the extent of the ASI network forecast. The description of the validation ground dataset is shown in Table 6.

Data type	Parameter	Locations	Start	End	Duration	filtering
Training	GHI	OLUOL, OLDON	Forecast instance - 30 days	Forecast instance	1 month	Solar elevation > 20°
Validation	GHI	OLCLO, PVAMM	2020-08-01	2020-08-31	1 month	Solar elevation > 20°

Table 6. Validation ground dataset

4.3 Methodology

4.3.1 Description

In order to combine the different forecasts sources, we have developed the method depicted in Figure 9.

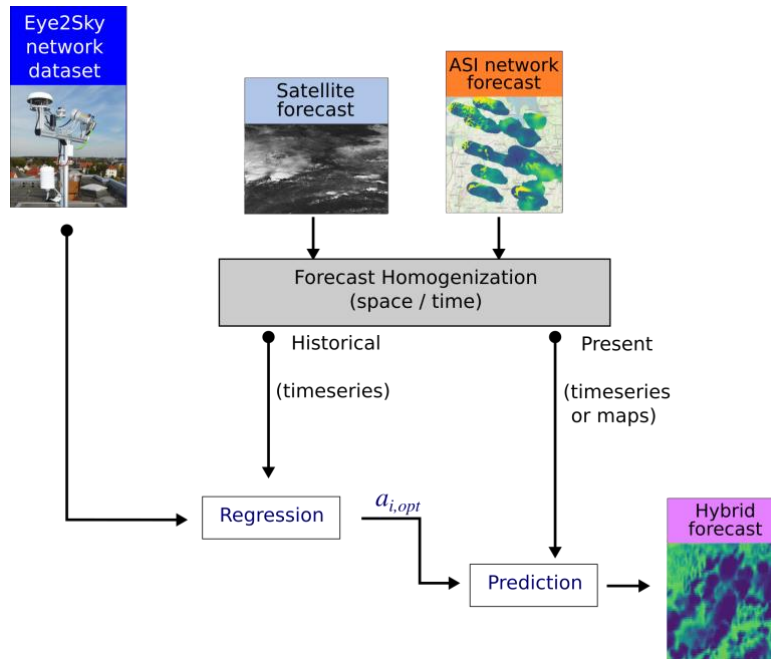


Figure 9. Combination model

The developed model is composed of 3 different blocks: homogenization, regression and prediction. In the homogenization block the forecast inputs are all converted into to the same spatio-temporal resolution. This process depends on the type of data needed (timeseries or maps). Once this homogenization is done, historical forecast timeseries are fed into the regression block. The number of timeseries used depends on the number of sites available with ground irradiance measurements. In this step, the **historical** forecasts are used as features and the ground measurements are used as samples (references) of a linear regression. The cost function of the regression is the linear combination of the forecast inputs. The more historical data is used, the more constraints and complexity are added to the system regarding the meteorological conditions. If too few days are used, the system will not have sufficient information to indirectly characterize the prevailing local atmospheric conditions (e.g., prevailing sky condition, aerosol content). If too many days are used, the regression will tend to overfit the prevailing conditions. The regression will output the optimum weights that each of the input sources will have plus a bias correction term. One regression will be performed independently per lead time. This means that for every forecast instance processed, there will be NS regressions performed, where NS is the number of forecast steps selected for the output of the combined forecast. In our specific case $NS = 30$ (1 forecast lead time per minute for 30 min). The regression block will output $NS \times NF + NF$ optimal weights, where NF is the number of forecast inputs combined (2 in our case). The “+ NF ” term accounts for the bias terms. Finally, the optimal weights found are used on the prediction block to combine the input **present** forecasts (and not **historical**). Here the combination can be indifferently applied to timeseries or maps. At the end of this process, we get the hybrid forecasts with the chosen spatial and temporal resolutions. In the following subsections a detailed description of the 3 model blocks is presented.

4.3.2 Forecast homogenization

In the forecast homogenization block, all forecast inputs are converted into a common spatial and temporal resolution. Here below we describe the different processes used on this homogenization step.

Spatial homogenization: when working with maps, first a projection and a spatial grid for the hybrid forecast must be chosen. In a first step, all data inputs are converted into the hybrid projection. Then the data is interpolated (to higher resolutions) or averaged (to lower resolutions) into the chosen hybrid spatial grid. Here the interpolation methods vary depending on the source forecast converted. When working with timeseries, the sites (coordinates) of interests are directly interpolated in the original forecast source projection and outputted directly to the other blocks of the model. In this work, we trained the linear regression weights(?) and validated the forecasts(?) using these timeseries.

Temporal homogenization: when working with different forecasts, there are 2 different temporal resolutions that could differ, the forecast update resolution (between 2 forecast instances) and the forecast step (between 2 forecast lead times). These types of interpolations are exemplified in Figure 10.

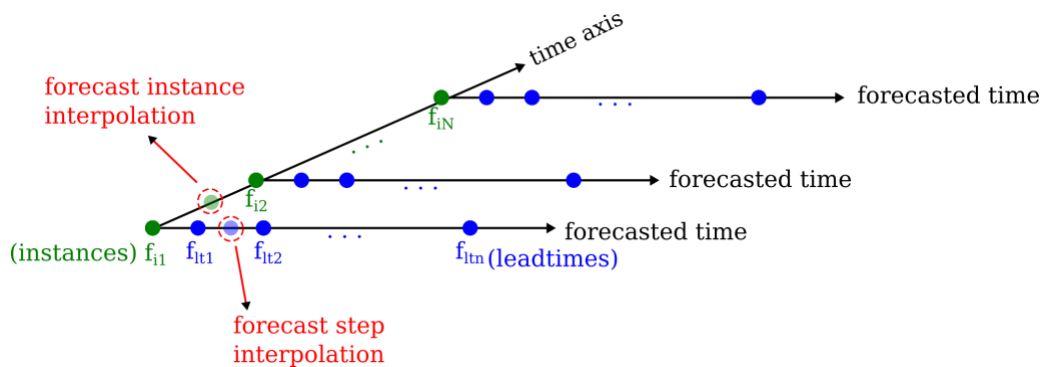


Figure 10. Forecast step and forecast instance interpolations.

In the method developed here, a linear interpolation within the last available forecast instance on the respective source is used to interpolate both interpolation types. This is quite straight forward for the forecast step interpolation but a little less intuitive for the forecast instance interpolation. All forecasts will have missing forecast instances with respect to the higher resolved one. In order to interpolate a missing instance, from the last available forecast instance the missing instance and all subsequent missing lead times are linearly interpolated. With this method the last interpolated lead time will be undefined as it will be a point outside the forecast horizon of the last available forecast instance. With the data available on this method, we found that this is the most accurate approximation of the unknown forecast instances.

4.3.3 Regression and prediction

Once the forecasts are homogenized, we can proceed to define the combined forecasts **per lead time** as the linear combination of the inputs forecasts sources, that is:

$$C = \sum_{n=0}^{N-1} (a_n \cdot F_n) + b \Big|_{\text{per leadtime}}$$

Where :

C = combined forecasted product
 F_n = Input forecast source n
 a_n = weight for forecast source n
 b = bias term
 N = number of input forecast sources

The basic principle is then to find the optimum weights a_n and b per lead time that minimize the **squared error** of this linear combination of forecasts using as reference the GHI measured with the ground measurement stations (linear regression). Here we see that the training is not performed on forecast maps but on forecast timeseries as the reference data does only exist on point-wise basis. In order to include indirectly the inertia of the local atmospheric conditions (e.g., aerosols), a fixed period d of historical forecast days is used on the training. The training can then be defined per lead time as

$$\min \left(\sum_{n=0}^{N-1} (a_n \cdot \bar{F}_n) + b - \overline{GHI} \right) \Big|_{\text{per leadtime}}$$

Where:

\bar{F}_n = array of forecasted pixels for source n of length $d \cdot s$ (features)
 \overline{GHI} = array of GHI measurements of length $d \cdot s$ (samples)
 d = number of historical days
 s = number of available measurement sites
 a_n = weight for forecast source n
 b = bias term
 N = number of input forecast sources

Form the regression we obtain the optimized weights a_n and optimized bias term b per lead time.

Once the training phase is done, we can proceed with the linear combination of the **present** forecasts per lead time using the optimized weights a_n and optimized bias term b . As a result, we obtain a unique combined forecast with the highest temporal and spatial resolutions. These optimized coefficients can be either applied map-wise or point-wise, so the output of the combination can be either forecasted maps or forecasted timeseries.

4.4 Evaluation

The sources combined in this evaluation are the Satellite and ASI network forecasts. These 2 sources are jointly available from the 01.07.2020 to the 31.08.2020 (see Table 5). The training of the regression was performed using 2 sites on the Eye2Sky network, **OLUOL** and **OLDON** (see Figure 2 and Table 6). The regression was performed with a historical forecast dataset of 30 days. This time range was found to be the period in which improvement of error metrics were maximized, as shown also in Kühnert, J., 2016. Due to this, the first forecasted day from the combined method is the 01.08.2020 and the last is the 31.08.2020. The characteristics of the obtained hybrid forecast are shown in Table 7.

Parameter	Combined Satellite + ASI network forecast
Spatial resolution	Evaluated directly on time series
Forecasts update	1 min
Forecast step	1 min
Forecast horizon	30 min
Availability	01.08.2020 to 31.08.2020
Parameter	GHI
Type	Deterministic

Table 7. Characteristics of the obtained Satellite + ASI network forecast.

The validation of the hybrid forecast was performed using the sites **OLUOL** and **OLDON** (see Figure 2) with the forecasts obtained from 01.08.2020 to 31.08.2020. The error metrics used on this evaluation are the Root Mean Squared Error (RMSE) and Mean absolute Error (MAE). The KPI used for this task is the KPI1.1.a : 10-15% RMSE improvement up to 30 min ahead (see complete list of projects KPIs in Appendix A).

4.5 Results and Discussion

4.5.1 Benchmarking of the input forecasts on the Eye2sky region

To set the basis for the validation of the combined forecast, we first study the performance of the individual input forecasts on the Eye2sky domain. Figure 11 shows the validation of the satellite forecasts on the 2 summer months of the study (01.07.2020 to 31.08.2020). Here, we have used all the available ground measurement stations of the Eye2Sky network.

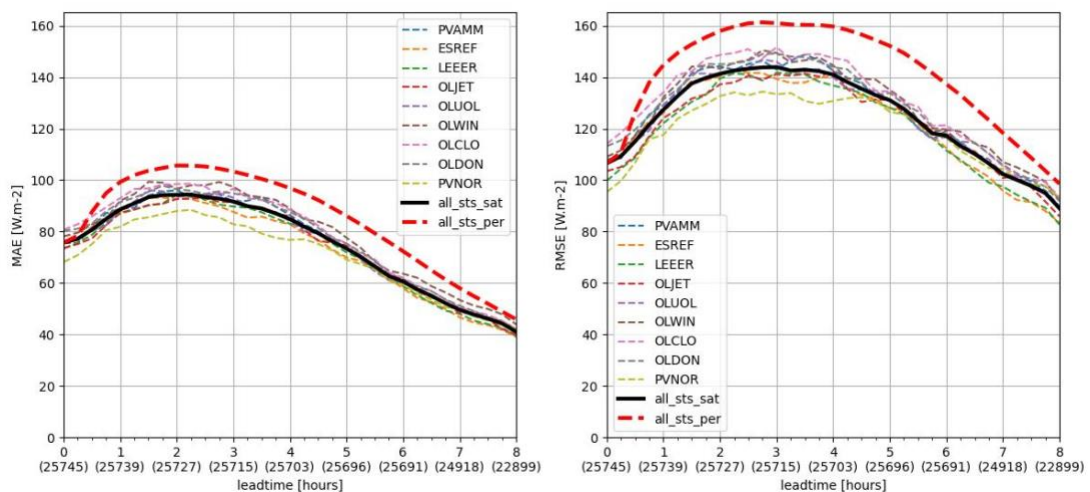


Figure 11. Validation of the satellite forecast on the Eye2sky domain. (01.07.2020 to 31.08.2020)

In this figure we see the absolute MAE and RMSE for the 8 hours lead time every 15 min. Results are shown for the individual stations (dashed lines) and for the aggregation of all station together (thick solid line). By aggregation here we mean aggregating all the irradiance values together and then determine the RMSE. As a reference we also include the aggregated satellite persistence (thick dashed line). First, we see that for all stations individually and the

aggregated values, the RMSE and MAE of the satellite forecast improves compared to persistence for most of the lead times. The best improvement for the aggregated on MAE is 13.19 W/m² and on RMSE is 23.39 W/m² on the lead time 5h45m. Only for the very low lead times this is not the case as persistence is usually the best forecast in this case. The error metrics for the lower lead times (~78 W/m² for MAE and ~110 W/m² for RMSE) are expected and comparable with other type of satellite forecast methods (Polo, J., 2008). In the parenthesis under the lead times we see the amount of valid points used to calculate the error in each lead time. We see that the available data decreases with lead time, mainly due to fact that as lead time increases, the probability of night values increases as well. We also see that for high lead times the errors tend to improve (decrease) which is counter intuitive. This is an artifact that comes from the fact that at high lead times we find a high probability to be on the afternoon irradiance values. These irradiance values are small, so the probability to have an error decreases when validating these low values. To avoid this, we also show the relative error metrics in Figure 12. In this figure we see the expected behaviour of a forecasts in which the error metrics increases with lead time. The find as before a maximum improvement on lead time 5h45m of 6.97% for MAE and 12.37% for RMSE. These values set up the reference to which we can compare the other forecasts.

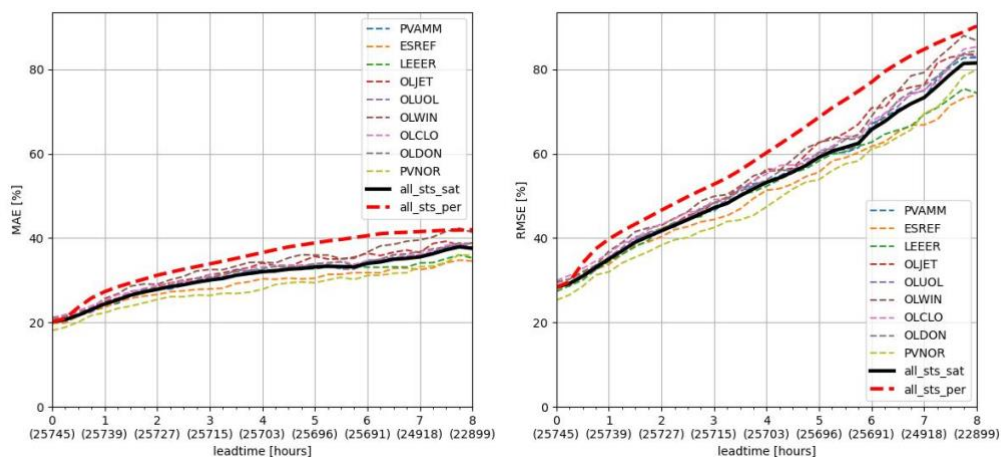


Figure 12. Validation of the satellite forecast on the Eye2sky domain using relative error metrics. (01.07.2020 to 31.08.2020)

We now continue with the validation of the ASI network irradiance forecast in the 40 km by 40 km extent around Oldenburg area (see Table 5) on the same 2 summer months. This validation is shown in Figure 13. Here we can only use the 5 ground measurement stations inside the ASI network forecast extent. First, we see that for the lower lead times, the MAE (~54 W/m²) and the RMSE (~100 W/m²) of the ASI network forecasts show already an improvement to the satellite forecast for the same test case (improvement of 21.78 W/m² for MAE and 7.4 W/m² for RMSE). Also we see that the errors for the station OLDON are quite low. This is because the irradiance values from this station are used as part of the irradiance estimation of the ASI network forecasts (see Section 3.3.2). We also see that for higher lead times, the error metrics reach a plateau that seems to stabilize the error on a fix value. This is another artifact also caused by missing data. Indeed, the ASI network forecasts are quite limited in extent (40 km x 40 km) and have no information of the cloud situation outside its boundaries. So when the clouds move through and out of the forecast extent with no information coming in from the

outside, some pixels are left with undefined values. As lead time increases, so does the amount of undefined pixels in the forecast extent.

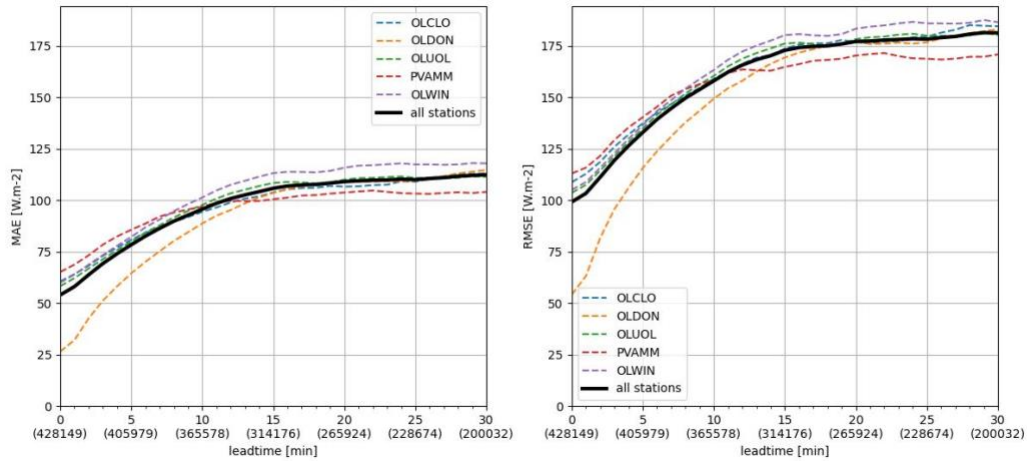


Figure 13. Validation of the ASI network forecast on the Eye2sky domain (01.07.2020 to 31.08.2020).

This is exemplified for an extremely unfavourable case in Figure 14. Here we have a situation with low clouds under strong Southwest wind. For lead time 0, we see that all 5 station pixels have a defined irradiance value. As lead time increases, the clouds (irradiance information) move rapidly towards the Northeast. At lead time 14, 2 stations are already outside the validity domain. At lead time 20, all measurement station pixels are outside. This means that from minute 20 onwards all points of interest in this test case will be undefined.

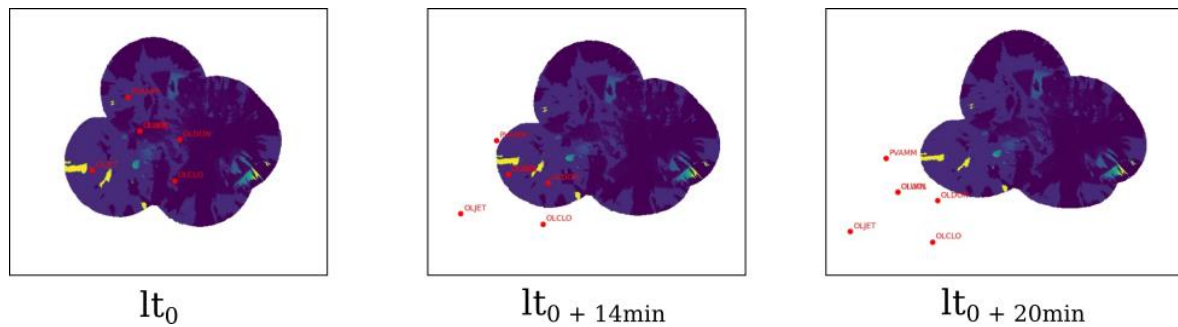


Figure 14. Undefined values encountered on the ASI forecast domain for an extremely unfavorable case (low cloud height with strong winds).

In order to avoid this artifact on the ASI forecast, the points that are left undefined are filled with a type of persistence that takes partly into account the variability of the situation. This persistence is defined as:

$$GHI[idx_{nan}] = \text{mean}(GHI[\sim idx_{nan}])$$

where idx_{nan} are the indices of the forecast pixels where the GHI value is left undefined.

4.5.2 Benchmarking of the combined Satellite + ASI network forecast on the Eye2sky region

For the benchmarking of the combined Satellite + ASI network forecast, we compare the different error metrics of this new developed forecast with the ones found for the satellite persistence, satellite, and ASI network forecasts. These results are shown in Figure 15.

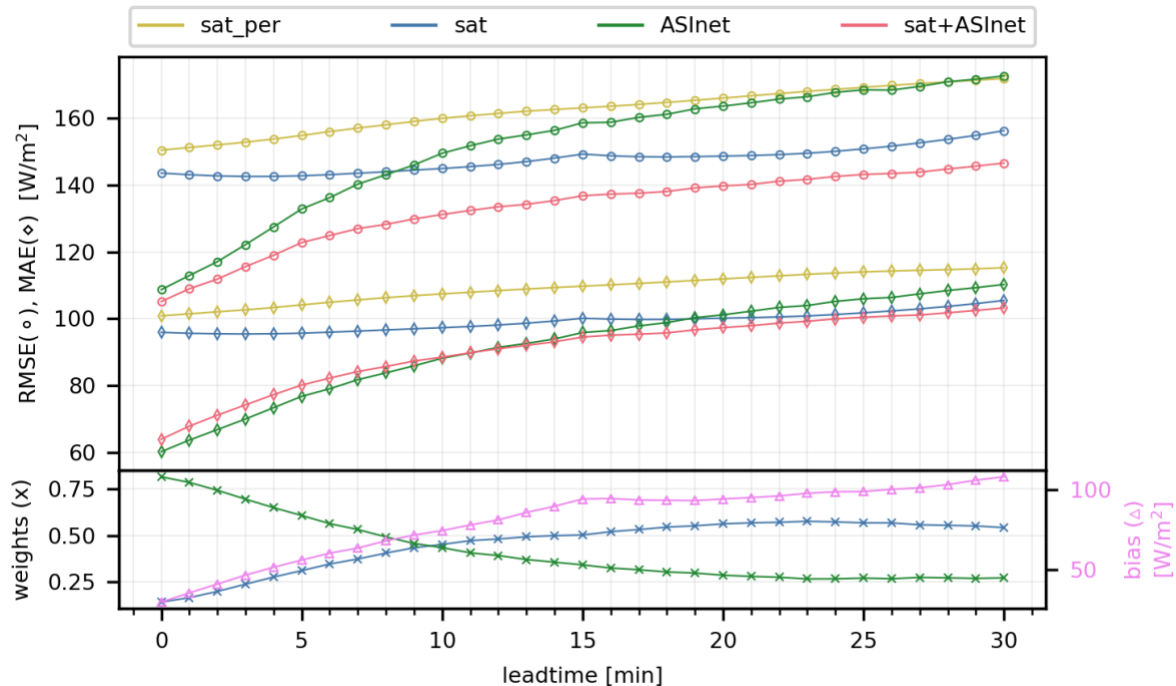


Figure 15. Benchmark for the combined forecast on the nominal synchronization case. **Top:** Error metrics RMSE(°) and MAE(◇). **Bottom:** average optimized combination weights(x) and optimized combination bias term (△) in the secondary axis.

In this figure we see that as expected the satellite persistence and satellite forecasts present a low variability on this relative short lead time (30 min) and that the satellite forecast always outperforms the satellite persistence. On this point, it is quite strange to see that the satellite persistence and the satellite forecast error metrics differ from one another on lead time 0. This is explained by the interpolation of the missing forecast instances (see Section 4.3.2). If we only use the non-interpolated forecast instances (on minutes 0, 15, 30 and 45) we get the expected behaviour where both satellite-based forecasts show the same error metrics at lead time 0. All other intermediate minute values are interpolated from the last available satellite and satellite persistence forecast instances respectively. As the first forecasted value (lead time 15) for both sources are different, thus also their interpolations between 1 and 14 minutes. So at lead time 0, the values for the intermediate forecast instances will be different for each source. Due to this, there will be a difference in the error metrics at lead time 0 when computing the metric for the aggregation of all (interpolated and non-interpolated) values together. As explained before, this is the most accurate approximation of the unknown forecast instances. This difference is still small (6.8 W/m² for RMSE and 4.9 W/m² for MAE) and does not affect the overall results of the entire benchmark.

The satellite forecasts also seem to have a slight improvement between lead times 0 to 15 and also again from 15 to 30 (U shape response). This is an artifact that comes from the other type of interpolation, the forecast step interpolation (see Section 4.3.2). In this case the interpolation has an averaging effect that translates in a slight improvement of the error metrics for the interpolated values.

We see that the RMSE of the ASI network outperforms the RMSE of the satellite forecast until lead time 8. This comes from the fact that the ASI network forecast has a much higher spatio-temporal resolution, which translates into a finer description of the cloud situation. This will result into a more accurate estimation of the irradiance at a local level. As explained in the previous section, this advantage will be reduced as lead time increases (as clouds move through the forecast extent) because no new information from the cloud situation is known outside the ASI network extent. This means that on average the cloud information contained in the ASI network forecast after 9 min deviates from the real cloud conditions in such a way that it can not produce such accurate forecasts anymore. We see that at lead time 30 the RMSE of the ASI network and the satellite persistence are very similar. This implies that for this particular case, the ASI network forecast will contain valuable cloud information until this limit of 30 min. A similar behaviour is found for the MAE with the cross point on lead time 19.

Looking now into the combined satellite + ASI network forecast, we find a significant improvement of the RMSE with respect to both input forecasts. In general, the combined forecast RMSE outperforms all forecasts for all lead times, with a maximum improvement of 10.36 % at lead time 8. Table 8 shows the RMSE per forecast method and the improvements of the combination with respect to the individual satellite and ASI network forecasts. From the table we see that the RMSE improvement between 5 and 30 min with respect to the satellite forecast ranges from 5.07% to 13.97% and with respect to the ASI network from 7.55% to 15.09%. Even when we take the lowest improvement per lead time into account against both forecast inputs (underlined values), we get an overall improvement that ranges from 5.07% - 10.36% (at lead time 8). In any of these 3 cases the improvements for RMSE of 10%-15 % defined on the KPI 1.1.a are satisfied (See Appendix A for complete list of projects KPIs).

Leadtime [min]	Sat [W/m ²]	ASInet [W/m ²]	Sat+ ASInet [W/m ²]	Improvement of Sat + ASInet over only SAT [%]	Improvement Sat + ASInet over ASInet[%]
0	143.52	108.72	105.16	26.72	<u>3.27</u>
5	142.71	132.81	122.78	13.97	<u>7.55</u>
10	144.89	149.45	131.15	<u>9.48</u>	12.24
15	149.19	158.54	136.74	<u>8.35</u>	13.75
20	148.59	163.52	139.68	<u>6.00</u>	14.58
25	150.75	168.38	143.10	<u>5.07</u>	15.01
30	156.18	172.55	146.52	<u>6.19</u>	15.09

Table 8. RMSE per forecast for selected lead times + relative improvement of nMAE of Satellite + ASInet over only SAT and only ASInet. The underlined values represent the minimum RMSE improvement per lead time taking both forecast inputs into account (worst case improvement)

The MAE of the combined forecast has a different trend. From Table 9 we see that it has clearly improved over the satellite forecast, starting with an improvement of 33.28% down to 1.30% at lead time 25. The case is much different with respect to the ASI network forecast, where we find an under performance starting with -6.17% that goes until lead time 11. Then the MAE of the combination will outperform the ASI network forecast with a maximum value of 6.35% at lead time 30. The reason for the different behaviour between the RMSE and MAE is that the

combination method itself has been designed to minimize the **squared error** of the linear combination of the input forecasts (see Section 4.3.2). Thus the combination is optimized to minimize the RMSE (itself an squared error) and not the MAE (itself a linear error). This choice is based on the fact that the RMSE is the most common used metric for the validation of these types of forecasts (e.g, RMSE is the metric chosen in the KP1 1.1.a).

In Figure 15 we also find the average optimized weights per lead time that each of the input forecast received on the combination (bottom figure). It is clear that on average the combination learned that for lower lead times the ASI forecast information has a higher weight (describes more accurately local cloud situation and hence the irradiance values). For this test case the ASI forecast will dominate the combination until lead time 9, where the weight values cross. From lead time 10 onwards the satellite forecast will provide the highest contribution. This shows that the hybrid forecast learns to take advantage of the individual strengths of each input forecast, to result in a product that is nearly the best of both worlds. The location of this cross point should be site dependent.

Leadtime [min]	Sat [W/m ²]	ASInet [W/m ²]	Sat+ ASInet [W/m ²]	Relative Improvement of Sat + ASInet over only SAT [%]	Relative Improvement Sat + ASInet over ASInet[%]
0	95.95	60.31	64.02	33.28	<u>-6.17</u>
5	95.71	76.84	80.22	16.19	<u>-4.40</u>
10	97.35	88.22	88.56	9.03	<u>-0.38</u>
15	100.16	95.91	94.55	5.60	1.41
20	100.20	101.19	97.37	<u>2.83</u>	3.78
25	101.79	105.98	100.47	<u>1.30</u>	5.20
30	105.49	110.26	103.26	<u>2.12</u>	6.35

Table 9. MAE per forecast for selected lead times + relative improvement of nMAE of Satellite + ASInet over only SAT and only ASInet. The underlined values represent the minimum MAE improvement per lead time taking both forecast inputs into account (worst case improvement)

As discussed in Section 4.5.1, the ASI network forecast horizon is panellized by low clouds. In locations like the Eye2Sky network (North west Germany) which presents a sky dominated by low clouds, the ASI network performance decreases rapidly with lead time. This results on a minimization of the contribution of the ASI network on the combined forecasts. For locations dominated by higher clouds, this cross point should appear on higher lead times. To corroborate this effect, the DLR is assessing the possibility of applying the combination method on the Plataforma Solar de Almeria, which has 5 ASIs installed on its perimeters.

Finally, the combination method finds at the same time a bias correction, represented by the free term on the linear combination (see Section 4.3.2). The optimized average bias term obtained per lead time is shown in Figure 15 (bottom, secondary axis). We see that the bias correction ranges from 29.76 W/m² at lead time 0 to 108.06 W/m² at lead time 30. The bias correction term also shows the u-shape like response found on the satellite forecast terms. This seems to imply that the satellite forecast introduces the highest bias deviation to the combined product and that the method itself tries to compensate for this directly on the regression.

4.5.3 Benchmarking of the performance of the forecasts with respect to the variability condition

The results in the previous section do not allow a differentiation of the error metric performance on the prevailing meteorological conditions (e.g. different cloud situations). In order to achieve this, a benchmark of the forecasts on prevailing irradiance variability conditions was performed. The variability conditions are here defined by the variability index (VI) developed in (Marquez, R., 2013). This variability index is defined as the standard deviation of the clear sky index increments $\Delta k^*(t)$, as

$$VI = \sqrt{\frac{1}{N} \sum_{i=1}^N [\Delta k^*(t_i)]^2} = \sqrt{\frac{1}{N} \sum_{i=1}^N [k^*(t_i + \Delta t) - k^*(t_i)]^2}$$

Where:

k^* = clear sky index

$\Delta k^*(t) = k^*(t + \Delta t) - k^*(t)$ (clear sky index increment)

Δt = step of the increment (time difference)

$i = \{0 \dots N\}$ = forecast instances taken into consideration in the VI

A closer look to the obtained VI equation evidences that by definition the VI has the same formulation of the RMSE of the k^* persistence

$$VI = \sqrt{\frac{1}{N} \sum_{i=1}^N [k^*(t_i + \Delta t) - k^*(t_i)]^2} = RMSE_{k^* persistence}$$

as for any change $t_i + \Delta t$, the persistence forecast will give the value at t_i . Using a VI in terms of the clear sky index allows us to dissociate the deviations due to the daily irradiance pattern from our metrics.

For this benchmark, the variability index is calculated using the ground persistence clear sky index (k_{gnd}^*) on a sliding window of 25 forecast instances (N=25 min/forecast instances) throughout the month of 08.2020. The sites used here are the same 2 validation sites, **PVAMM** and **OLCLO**.

In Figure 16 the average RMSE of the clear sky index for each one of the benchmarked forecasts in terms of VI is shown (VI depicted with bins of length 0.02). In this figure we show the performances of the forecasts for an increment step Δt of 5 min (or lead time 5). First of all, we see that per definition, the RMSE of the ground persistence falls exactly in the diagonal. All values under the diagonal mean an improvement over ground persistence and vice versa. In the secondary index (+) we see the relative cumulative sum of the available points per bin.

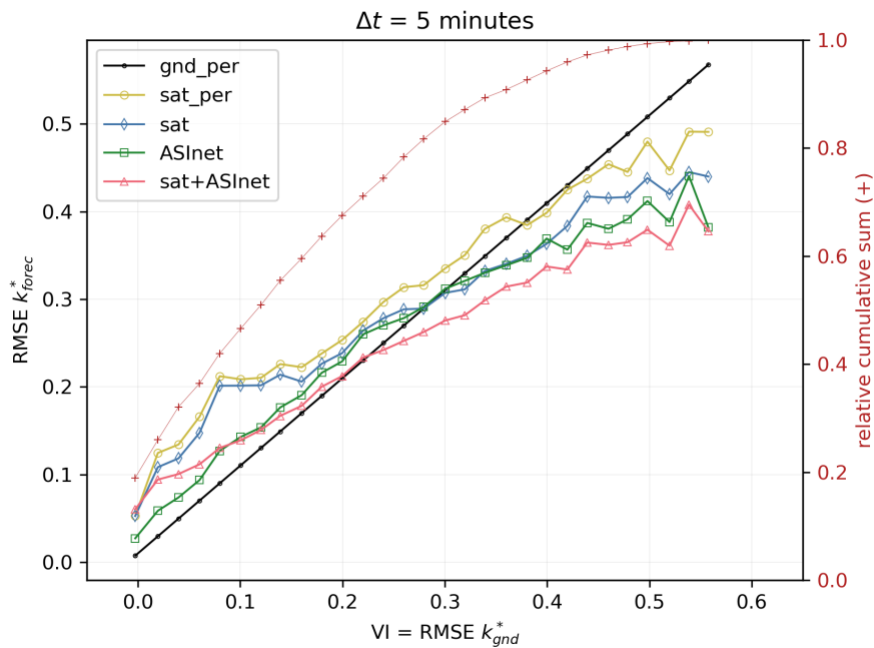


Figure 16. Average RMSE of k_{forec}^* in terms of the variability index (VI) for $\Delta t = 5$ min and $N=25$ min (bin width = 0.02). The forecasts shown are ground persistence (\cdot), satellite persistence (\circ), satellite (\diamond), ASI network (\square) and combination of satellite and ASI network (Δ). On the secondary axis the relative cumulative sum of the available points (+)

We see that as the variability increases, so does the RMSE for all forecasts (as expected). The difference between the forecasts comes from the steepness of the growth gradient of the RMSE. It is important to note that for all VI values ≥ 0.2 , the combination forecast shows the lower RMSE compared to all other forecast sources.

Almost 20% of the points fall directly on the $VI=0$, which translates to clear sky or overcast conditions. For this VI value the ground persistence presents the better performance, that is, a negative forecast skill for all forecast sources (which is also expected). The least negative forecast skill is shown by the ASI network, followed by the satellite, combined forecast and satellite persistence with a very similar value.

In order to facilitate the comparison with the ground persistence source as a reference, the difference between the RMSE k_{forec}^* and RMSE k_{gnd}^* is shown from Figure 17 onwards. For the studied increment step ($\Delta t = 5$), the combination forecast presents a positive forecast skill from conditions with a $VI \geq 0.2$, while for the ASI network, satellite and satellite persistence the values are 0.28, 0.28 and 0.38 respectively. This shows that the combined forecasts present the lowest average RMSE on high variability situations compared to the individual input forecast sources.

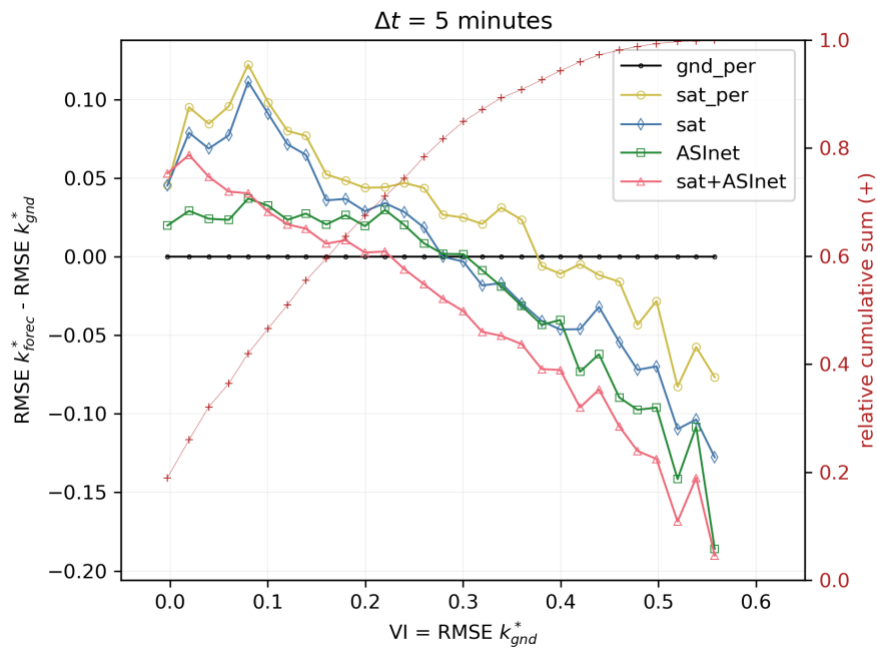


Figure 17. Difference of average RMSE k_{forec}^* with the average RMSE k_{gnd}^* in terms of the variability index using $\Delta t = 5$ min and $N=25$ min (bin width = 0.02). The forecasts shown are ground persistence (\cdot), satellite persistence (\circ), satellite (\diamond), ASI network (\square) and combination of satellite and ASI network (\triangle). On the secondary axis the relative cumulative sum of the available points (+)

For a more general view of the performance of the combined forecast in terms of variability, the same study as before is shown in and Figure 19 for the increment steps Δt from 0 to 17 min.

For the case of $\Delta t = 0$, we retrieve the RMSE found on the analysis case (with no forecast). As expected, the best performing source is persistence (RMSE=0) followed by ASI network, combined forecast, satellite and satellite persistence. As Δt increases, the higher variability conditions begin to appear. On the case with $\Delta t=1$ minute, the variable conditions are found only until VI of 0.22. Here still all forecasts show a negative skill (difficult to outperform persistence in such a low lead time). At $\Delta t=2$, the variable conditions are found until a VI of 0.4 and the forecasts begin to show a positive skill, from VI=0.3 for the combined forecast and VI=0.32 for the ASI network. The other forecast sources still present a negative skill in such low lead times. From $\Delta t=3$ to $\Delta t=6$, the higher variability conditions start to appear (VI from 0.46 to 0.58) and the VI cross points in which the forecasts start to have a positive skill begin to decrease. From $\Delta t=7$ onwards, the performances of the different forecasts begin to stabilize with the most performant forecast being the combined satellite + ASI network forecast for variability conditions from VI ≥ 0.16 . This higher performance on high variability conditions is one of the main research objectives set up in the beginning of this project task. For this test case, it is found that from the variability perspective, conditions get stabilized after 7 min. This is also the increment step ($\Delta t = 7$) in which the high variability dependent errors of the satellite forecast equalize the performances of the ASI network (as seen in the $\Delta t = 7$ subfigure in). This is an indication that on average the ASI network forecast is able to contribute to the minimization of high variability dependent errors of the combined forecast until lead time 7. After this, it is the satellite behaviour that prevails.

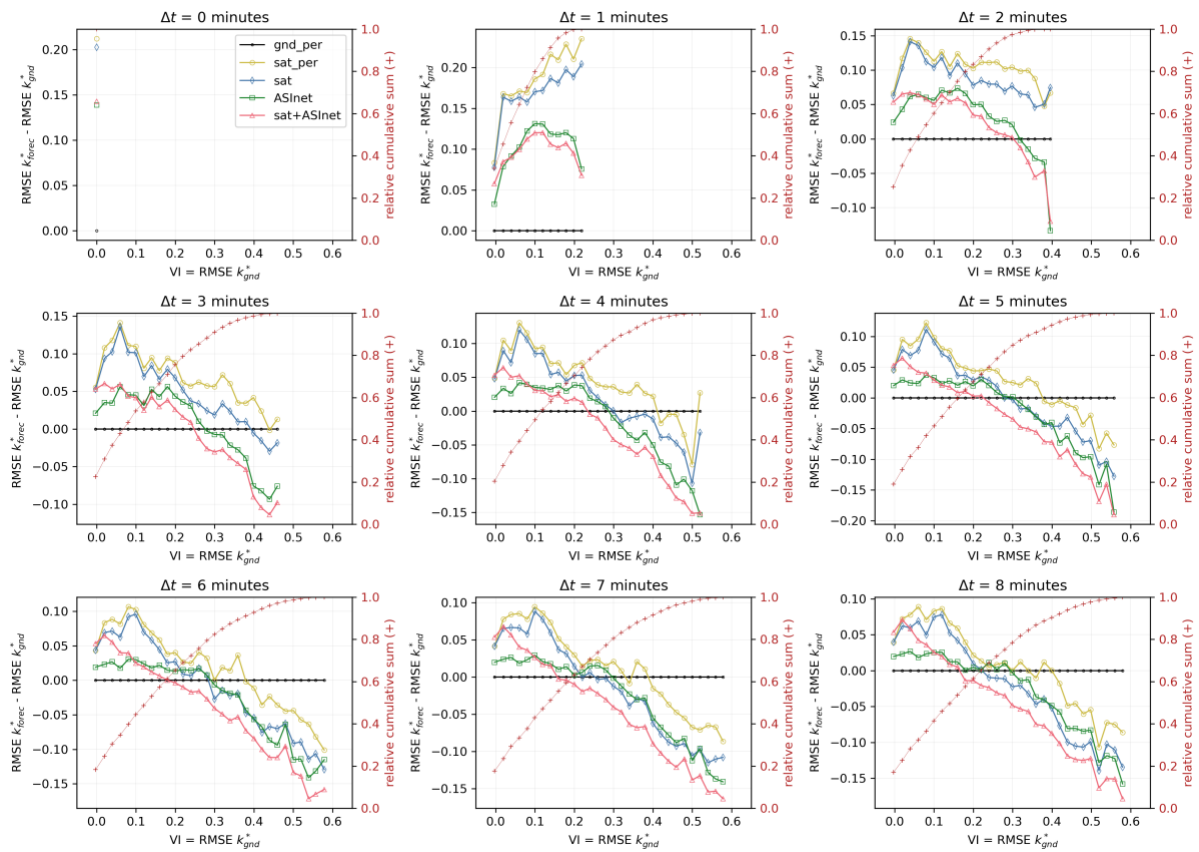


Figure 18. Difference of average RMSE k_{forec}^* with the average RMSE k_{gnd}^* in terms of the variability index bins (bin width = 0.02) using $N=25$ min. Each figure represents a value of Δt from 0 to 8 min. The forecasts shown are ground persistence (-), satellite persistence (o), satellite (\diamond), ASI network (\square) and combination of satellite and ASI network (\triangle). On the secondary axis the relative cumulative sum of the available points (+)

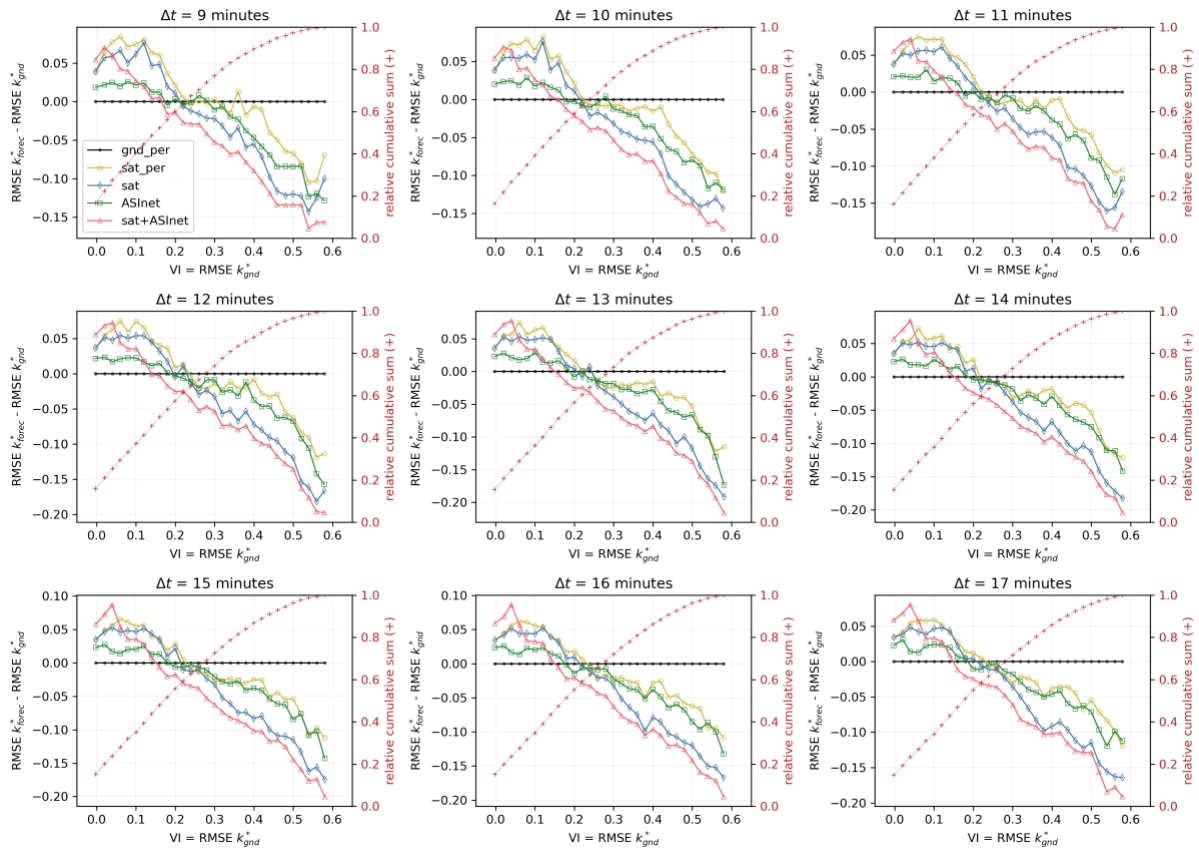


Figure 19. Difference of average RMSE k_{forec}^* with the average RMSE k_{gnd}^* in terms of the variability index bins (bin width = 0.02) using $N=25$ min. Each figure represents a value of Δt from 9 to 17 min. The forecasts shown are ground persistence (\cdot), satellite persistence (\circ), satellite (\diamond), ASI network (\square) and combination of satellite and ASI network (\triangle). On the secondary axis the relative cumulative sum of the available points (+)

4.5.4 Correlation of increments as a qualitative variability measurement

In the previous section we saw how the RMSE behaves on average for different variability conditions and that the RMSE of the combination forecast outperforms the other forecasts for high variability conditions. Now, on a further step we want to compare the different methods in their ability to forecast variations of irradiance (forecast of variability). For this we correlate the increments of the clear sky index of the forecast source (Δk_{forec}^*) to the increments of the clear sky index of the ground measurements (Δk_{gnd}^*) for the same increment step (Δt).

As we saw in the previous section, the lead times 1 to 4 have a low probability to present cases of high variability. So, the relative scatter density plot for a $\Delta t = 5$ min is shown in Figure 20. For the satellite persistence we see that all of the counts fall in the x-axis. That is expected as by definition the clear sky index persistence forecast will not be able to recognize any variations of Δk_{gnd}^* . As explained earlier, not all values of the satellite persistence forecast fall exactly into the x-axis because of the interpolation of the Δt forecast instances (see Section 4.5.2). In contrast, a perfect forecast will recognize all variations of Δk_{gnd}^* , thus resulting in all counts falling within

the diagonal line. The correlation for the satellite forecast improves over the persistence forecast but still shows semi-persistent behaviour. This can be explained from its low original time resolution which gives it a kind of persistence inertial behaviour when interpolated and compared with high resolution data. Nevertheless, we see that this forecast already concentrates a big part of its values towards the diagonal line. Also we see on this correlation the apparition of peripheral values (far from the diagonal and the origin [0,0]). Depending on the quadrant, this peripheral values relate to a sign error on the forecasted increment (quadrants II and IV) or a small time shift between the forecasted and the predicted increment (quadrants I and III). The ASI network correlation shows yet another behaviour with values falling on the y-axis ($\Delta k_{gnd}^* = 0$). These are related to the forecast of increments when there where no increments measured with the ground data. Also a higher density of points is seen on peripheral regions. These values can be attributed to the high temporal resolutions of the forecast, which increases the chances of predicting the increment with a time shift. Finally, the correlation of the combined forecast shows a clearer concentration of the values towards the diagonal, which is stronger than the ones of the satellite and ASI network forecasts. Also the probability of shifted increments decreases with respect to the ASI network forecast (density of the counts of the I and III quadrant). These are qualitative indications of a higher capability to forecast the correct increments (forecast variability) than the other forecasts.

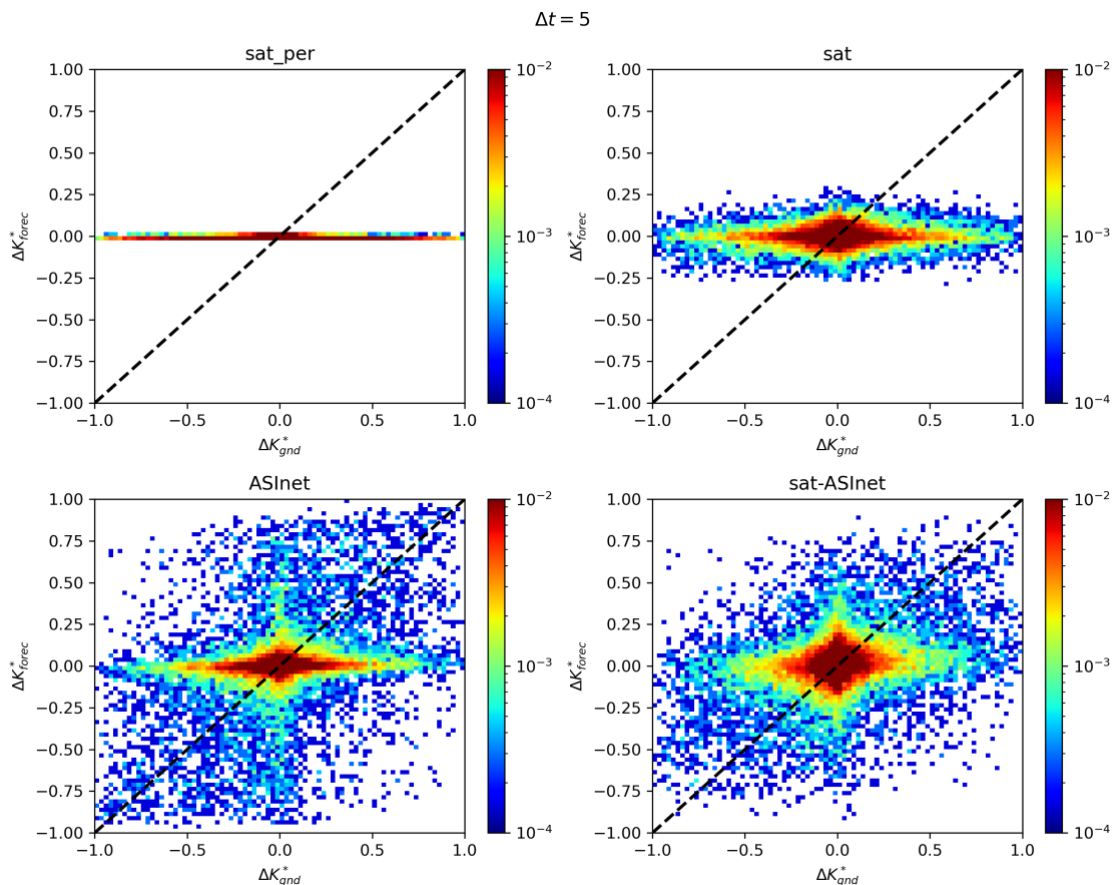


Figure 20. Relative scatter density plot of the increments of the clear sky index of the forecast source Δk_{forec}^* with the increments of the clear sky index of the ground measurements Δk_{gnd}^* for $\Delta t = 5$ min (the colors are in logarithmic scale).

5 Conclusion

Starting from a state-of-the-art ASI pair, an ASI network was developed in this work. The ASI network uses the intermediate products of ASI pairs and individual ASIs and combines them by dedicated statistical procedures. These intermediate products are cloud base height, segmented sky images (detected clouds), cloud velocity and diffuse irradiance estimated based on the ASI images. These combinations help to mitigate errors which are present in the intermediate products of individual ASIs and ASI pairs. As experimental infrastructure, the Eye2Sky ASI network with 23 operational ASIs located in an area of 110 km × 100 km was used. In the validation, the enhanced ASI-based nowcast proved to be more accurate than the state-of-the-art nowcast of an ASI pair and persistence. Depending on the evaluated station, the ASI network reduces RMSD by 23-30% ($35 - 50 \text{ W/m}^2$), 15-21% ($25 - 37 \text{ W/m}^2$), 12-16% ($20-27 \text{ W/m}^2$), 8-12% ($14 - 21 \text{ W/m}^2$) over persistence at evaluated lead times of 5, 10, 15, 20 min. The ASI network reduces deviations compared to the reference nowcasts especially if locations are evaluated which are more distant from the meteorological station which supports the nowcasts. As to be expected, both ASI-based nowcasts bring a larger improvement over persistence in more variable atmospheric conditions. In these more variable conditions, the ASI network reduces RMSD by up to 36% and up to 75 W/m^2 over persistence. The ASI network's nowcast was also analyzed for higher lead times. For lead times of up to 95 min, the ASI network exhibited a lower RMSD than persistence. In this range, RMSD is reduced by up to 21% and up to 25 W/m^2 over persistence.

Also in this work a method to combine the highly resolved ASI network forecast with the satellite based forecast was developed. The method uses a linear regression to combine optimally the forecast inputs in such a way that the average error metrics are minimized with respect to ground measurements. We found that this newly developed hybrid forecast outperforms the RMSE of persistence and the input forecasts for all lead times calculated. It shows an improvement in RMSE of 5.07% to 13.97% (7.65 W/m^2 to 19.93 W/m^2) with respect to satellite forecasts and 7.55% to 15.09% (10.03 W/m^2 to 26.03 W/m^2) with respect to the ASI network forecast on lead times going from 5 to 30 min. It also shows a lower RMSE on the clear sky index for highly variable conditions.

The work of this study is based on the Eye2Sky ASI network as it was available in the year 2020. With the ongoing extension of Eye2Sky, gaps in its spatial coverage are being closed. This will allow to develop an even more elaborate ASI-based nowcast for the higher lead times for which the data basis was not optimal yet in this study. From the forecast combination perspective, the processing of input data for more months during the year is needed to assess the seasonal transferability of the results. The combined forecast should also be validated at locations with different characteristics as the ones found in Northwest Germany in order to assess the differences on performance due to different weather conditions (dominant cloud situation, aerosol content, etc.). Finally, other interpolations and averaging strategies should be tested to minimize the artifacts introduced by the linear interpolations used in the method.

Both of the methods developed here by the DLR have a Technology Readiness Level (TRL) of 6. These forecasts have been tested and validated in the relevant environment, the Eye2Sky network in our case. In order to achieve TRL of 7, both methods should be optimized and tested in operational use. This requires funding and collaboration with industrial partners and interested stakeholders. DLR is already in discussions with industrial forecast/hardware providers as well as with PV park owners and power traders to set up research projects that will allow such a TRL improvement.

The results of this work package have led to a number of journal articles (Blum et al. 2021, Nouri et al. 2021, Blum et al. 2022, Fabel et al. 2022). Further publications based on the outcomes summarized in this report are planned soon.

6 Key messages and recommendations

- The accuracy of ASI-based nowcasting can be increased notably by combining individual ASIs or ASI pairs into an ASI network.
- The combination of the ASI-based nowcasting with the satellite-based forecast can increase even further its initial accuracy.
- The nowcasts of an ASI network can be particularly useful for grid operators and energy traders as the spatial coverage of the ASI-based nowcast can be increased to cover e.g., a whole urban area. Further, a larger forecast horizon can be achieved as more ASIs at larger distances are included.
- The decision-making strategies from stakeholders of the energy market could benefit directly from the increased accuracy achieved with the combination of the ASI network nowcast with the satellite-based forecast, as higher forecast accuracy correlates with lower investment risk.

7 Bibliography

- Aides, A., A. Levis, V. Holodovsky, Y. Y. Schechner, D. Althausen and A. Vainiger (2020). Distributed Sky Imaging Radiometry and Tomography. 2020 IEEE International Conference on Computational Photography (ICCP), Saint Louis, MO, USA.
- Blum, N. B., B. Nouri, S. Wilbert, T. Schmidt, O. Lünsdorf, J. Stührenberg, D. Heinemann, A. Kazantzidis and R. Pitz-Paal (2021). "Cloud height measurement by a network of all-sky imagers." *Atmos. Meas. Tech.* 14(7), pp. 5199-5224, DOI: 10.5194/amt-14-5199-2021.
- Blum, N. B., S. Wilbert, B. Nouri, J. Lezaca, D. Huckebrink, A. Kazantzidis, D. Heinemann, L. F. Zarzalejo, M. J. Jiménez and R. Pitz-Paal (2022). "Measurement of diffuse and plane of array irradiance by a combination of a pyranometer and an all-sky imager." *Solar Energy* 232, pp. 232-247, DOI: <https://doi.org/10.1016/j.solener.2021.11.064>.
- Dumortier, D., (1995) "Modelling global and diffuse horizontal irradiances under cloudless skies with different turbidities", Final Report JOU2-CT92-0144, Daylight II 2
- Eumetsat (2012). "Conversion from Radiances to Reflectances for SEVIRI Warm Channels", Technical Report, EUMETSAT, 2012, <https://www-eumetsat.int>. Eumetsat-Allee 1, D-64295 Darmstadt, Germany
- Fabel, Y., B. Nouri, S. Wilbert, N. Blum, R. Triebel, M. Hasenbalg, P. Kuhn, L. F. Zarzalejo and R. Pitz-Paal (2022). "Applying self-supervised learning for semantic cloud segmentation of all-sky images." *Atmospheric Measurement Techniques* 15(3), pp. 797-809, DOI: 10.5194/amt-15-797-2022.
- Hammer, A., et al., (2003), "Solar energy assessment using remote sensing technologies", *Remote Sensing of Environment* 86, pp. 423–432. doi:10.1016/S0034-4257(03)00083-X
- Hammer, A.; Kühnert, J.; Weinreich, K.; Lorenz, E. (2015a) "Short-Term Forecasting of Surface Solar Irradiance Based on Meteosat-SEVIRI Data Using a Nighttime Cloud Index". *Remote Sens.* 7, <https://doi.org/10.3390/rs70709070>
- Hammer, A.; Kühnert, J.; Weinreich, K.; Lorenz, E. (2015b) „Correction: Hammer, A., et al. Short-Term Forecasting of Surface Solar Irradiance Based on Meteosat-SEVIRI Data Using a Nighttime Cloud Index." *Remote Sens.* 7, 9070–9090. *Remote Sens.* 7. <https://doi.org/10.3390/rs71013842>
- Jäger-Waldau, A., (2021), "Snapshot of photovoltaics – March 2021", *PJ Photovoltaics* 12, 2. <https://doi.org/10.1051/epjpv/2021002>
- Kuhn, P., B. Nouri, S. Wilbert, N. Hanrieder, C. Prah, L. Ramirez, L. Zarzalejo, T. Schmidt, Z. Yasser, D. Heinemann, P. Tzoumanikas, A. Kazantzidis, J. Kleissl, P. Blanc and R. Pitz-Paal (2019). "Determination of the optimal camera distance for cloud height measurements with two all-sky imagers." *Solar Energy* 179, pp. 74-88, DOI: 10.1016/j.solener.2018.12.038.
- Kühnert, J. (2016), "Development of a photovoltaic power prediction system for forecast horizons of several hours", PhD. Dissertation, Oldenburg University, Germany.
- Marquez, R. and Coimbra, C. (2013), "Proposed Metric for Evaluation of Solar Forecasting Models", *Journal of Solar Energy Engineering*, 135 (1):011016–011016. doi: 10.1115/1.4007496
- Mejía, F. A., B. Kurtz, A. Levis, Í. de la Parra and J. Kleissl (2018). "Cloud tomography applied to sky images: A virtual testbed." *Solar Energy* 176, pp. 287-300, DOI: 10.1016/j.solener.2018.10.023.
- Nouri, B., P. Kuhn, S. Wilbert, C. Prah, R. Pitz-Paal, P. Blanc, T. Schmidt, Z. Yasser, L. R. Santigosa and D. Heineman (2018). "Nowcasting of DNI maps for the solar field based on voxel carving



and individual 3D cloud objects from all sky images." AIP Conference Proceedings 2033(1), pp. 190011, DOI: 10.1063/1.5067196.

Nouri, B., P. Kuhn, S. Wilbert, N. Hanrieder, C. Prah, L. Zarzalejo, A. Kazantzidis, P. Blanc and R. Pitz-Paal (2019a). "Cloud height and tracking accuracy of three all sky imager systems for individual clouds." Solar Energy 177, pp. 213-228, DOI: 10.1016/j.solener.2018.10.079.

Nouri, B., S. Wilbert, L. Segura, P. Kuhn, N. Hanrieder, A. Kazantzidis, T. Schmidt, L. Zarzalejo, P. Blanc and R. Pitz-Paal (2019b). "Determination of cloud transmittance for all sky imager based solar nowcasting." Solar Energy 181, pp. 251-263, DOI: 10.1016/j.solener.2019.02.004.

Nouri, B., S. Wilbert, P. Kuhn, N. Hanrieder, M. Schroedter-Homscheidt, A. Kazantzidis, L. Zarzalejo, P. Blanc, S. Kumar and N. Goswami (2019c). "Real-Time Uncertainty Specification of All Sky Imager Derived Irradiance Nowcasts." Remote Sensing 11(9), pp. 1059, DOI: 10.3390/rs11091059.

Nouri, B., K. Noureldin, T. Schlichting, S. Wilbert, T. Hirsch, M. Schroedter-Homscheidt, P. Kuhn, A. Kazantzidis, L. F. Zarzalejo, P. Blanc, Z. Yasser, J. Fernández and R. Pitz-Paal (2020a). "Optimization of parabolic trough power plant operations in variable irradiance conditions using all sky imagers." Solar Energy 198, pp. 434-453, DOI: 10.1016/j.solener.2020.01.045 .

Nouri, B., S. Wilbert, N. Blum, P. Kuhn, T. Schmidt, Z. Yasser, T. Schmidt, L. F. Zarzalejo, F. M. Lopes, H. G. Silva, M. Schroedter-Homscheidt, A. Kazantzidis, C. Raeder, P. Blanc and R. Pitz-Paal (2020b). "Evaluation of an All Sky Imager Based Nowcasting System for Distinct Conditions and Five sites." AIP Conference Proceedings 2303(1), pp. 180006, DOI: 10.1063/5.0028670.

Nouri, B., N. Blum, S. Wilbert and L. F. Zarzalejo (2021). "A hybrid solar irradiance nowcasting approach: combining all sky imager systems and persistence irradiance models for increased accuracy." Solar RRL, pp. 2100442, DOI: 10.1002/solr.202100442.

Peng, Z., D. Yu, D. Huang, J. Heiser, S. Yoo and P. Kalb (2015). "3D cloud detection and tracking system for solar forecast using multiple sky imagers." Solar Energy 118, pp. 496-519, DOI: 10.1016/j.solener.2015.05.037.

Polo, J., Zarzalejo, L.F., Ramírez, L. (2008). "Solar Radiation Derived from Satellite Images" In: Badescu, V. (eds) Modeling Solar Radiation at the Earth's Surface. Springer, Berlin, Heidelberg. https://doi.org/10.1007/978-3-540-77455-6_18As

Remund, J., (2009) "Aerosol Optical Depth and Linke Turbidity Climatology", Description for Final Report of IEA SHC Task 36; Meteotest: Bern, Germany, Google Scholar.

Schroedter-Homscheidt, M., M. Kosmale, S. Jung and J. Kleissl (2018). "Classifying ground-measured 1 minute temporal variability within hourly intervals for direct normal irradiances." Meteorologische Zeitschrift 27, pp. 161-179, DOI: 10.1127/metz/2018/0875.

Sperati, S., (2016), "An application of the ECMWF Ensemble Prediction System for short-term solar power forecasting", Solar Energy, V. 133, pp. 437-450. <https://doi.org/10.1016/j.solener.2016.04.016>

Wang, G., B. Kurtz and J. Kleissl (2016). "Cloud base height from sky imager and cloud speed sensor." Solar Energy 131, pp. 208-221, DOI: 10.1016/j.solener.2016.02.027 <http://www.sciencedirect.com/science/article/pii/S0038092X16001237>.

8 Appendix A: Summary of Smart4RES KPIs

This Appendix summarises the KPIs defined in Smart4RES. These KPIs are divided in 2 groups:

- Project KPIs defined in the Description of Action
- Specific KPIs that are needed to evaluate technical results.

Please refer to Smart4RES Deliverable D.1.1 'Use cases, requirements and KPIs for RES forecasting', in particular Section 2.5 for a more detailed description of the different KPIs.

8.1 Project KPIs

8.1.1 Forecasting KPIs

KPI category	KPI index	KPI name	KPI baseline	KPI target
Weather Forecasting				
Project KPI	1.1.a	% absolute improvement Weather Forecasting score: 15 to 30 min ahead	Current operational solutions (AROME/ECMWF/GFS, DLR, EMSYS)	10-15% RMSE
Project KPI	1.1.b	% absolute improvement Weather Forecasting score: Few hours ahead	Whiffle forecast driven with ECMWF boundary conditions and without data-assimilation	10% RMSE
Project KPI	1.1.c	% absolute improvement Weather Forecasting score: From few hours to 96 hours ahead	Current operational solutions of MeteoFrance	10% RMSE, 4-6% CRPS (solar radiative) 5-10% CRPS (wind)
RES Forecasting				
Project KPI	1.2.a	% improvement RES Forecasting score: Up to 30 min ahead	Current operational solutions of EMSYS, EDP-R, errors from public datasets.	Solar: 9-12% RMSE, 3-5% CRPS Wind: 7-9% RMSE, 2-4% CRPS
Project KPI	1.2.b	% improvement RES Forecasting score: Up to 96 h ahead	Conditional evaluation on situations with highest forecasting errors.	Solar: 16-20% RMSE, 4-6% CRPS Wind: 12-15% RMSE, 3-5% CRPS
Specific KPI	1.2.c	% improvement Variogram score for ensemble forecasts	State-of-the-art methods for RES ensemble forecasts	≥ 0
Specific KPI	1.2.d	% improvement for seamless generic forecasts	Same as KPI 1.2.a, 1.2.b	Weighted combination of targets in KPI 1.2.a, 1.2.b over lead-times and RES sources

Table 10: Smart4RES Forecasting KPIs

8.1.2 KPIs on grid management applications

KPI category	KPI index	KPI name	KPI baseline	KPI target
Grid management applications				
Project KPI	1.3.a	% decrease of load shedding events in isolated power systems	Method without T5.2 tool and T5.1 storage support functions	>= 80%
Project KPI	1.3.b	% increased RES hosting capacity in MV distribution grids	Method without predictive management of flexibility from T5.3	>= 50%
Project KPI	1.3.c	Number of years in investment deferral in grid reinforcement	Traditional grid reinforcement	> 2 years
Specific KPI	1.3.e	Reduced energy curtailment of RES	Historical time series of RES production under curtailment conditions, without storage and innovative forecasting product	No target from the state-of-the-art. The objective is to minimize the KPI value
Specific KPI	1.3.g	Fulfillment of voltage limits	Traditional grid management without grid state optimization	No target from the state-of-the-art. The objective is to minimize the KPI value, computed in accordance with EN 50160
Specific KPI	1.3.h	Fulfilment of branch current limits		No target from the state-of-the-art. The objective is to minimize the KPI value
Specific KPI	1.5.a	Demonstration of a software-in-the-loop run using an example from the project	N.A.	Successful implementation of at least one Smart4RES use case as code and as a black box on a separate device
Specific KPI	1.5.b	Simulated environment including controls and interaction	N.A.	Successful interaction with the power system for at least one Smart4RES use case
Specific KPI	1.5.c	Test protocol to test for a least one potential risk	N.A.	Test of at least one potential risk of the software solution

Table 11: Smart4RES Grid management KPIs

8.1.3 KPIs on market applications

KPI category	KPI index	KPI name	KPI baseline	KPI target
Market applications				
Project KPI	1.3.d	% increase in electricity market revenue	Point forecasts and optimal quantile	10-15% decrease in costs stemming from balancing + 10-15% revenue from participation in energy plus ancillary services Up to 20-25% from VPP (RES and storage) in energy and ancillary services
Specific KPI	1.4.b	Analytic forecast evaluation by traders	Same as 1.3.d	Usual error levels observed by traders in similar conditions that chosen evaluation set
Specific KPI	1.4.c	'No-big-change' forecast evaluation by traders		
Specific KPI	1.3.f	Revenue losses per production unit due to curtailment	Historical time series of RES production under curtailment conditions, without innovative forecasting product	No target from the state-of-the-art. The objective is to minimize the KPI value

Table 12: Smart4RES Market applications KPIs



This project has received funding from the European Union's Horizon 2020 research and innovation programme under grant agreement No 864337